Advances in Engineering Software 53 (2012) 45–60

Contents lists available at SciVerse ScienceDirect

Advances in Engineering Software

journal homepage: www.elsevier.com/locate/advengsoft

Topology optimization of piezoelectric energy harvesting devices considering static and harmonic dynamic loads

Jin Yee Noh [a], Gil Ho Yoon [b,*]

[a] Application and Convergence R&D Team, Hyundai HYSCO, Republic of Korea
[b] School of Mechanical Engineering, Hanyang University, Seoul, Republic of Korea

ARTICLE INFO

Article history:
Received 14 October 2011
Received in revised form 20 July 2012
Accepted 25 July 2012
Available online 28 August 2012

Keywords:
Piezoelectric material with penalization
Static load
Harmonic load
Energy harvesting device
Structural optimization
Topology optimization

ABSTRACT

A topology optimization (TO) procedure is developed to design optimal layouts for piezoelectric energy harvesting devices (EHDs) by considering the effect of static and harmonic dynamic mechanical loads. To determine the optimal material distributions of a piezoelectric material considering the harmonic dynamic coupling effects between the electric energy and a structure for efficient EHDs, harmonic dynamic responses and the complex sensitivity analyses for various objectives related to the energy efficiency are calculated and derived. For the relaxation method of the density design variable for TO, material properties such as the anisotropic linear elasticity coefficients, piezoelectric coefficients, and permittivity coefficients are independently interpolated through the solid isotropic material with penalization (SIMP) approach with three penalization values. Through several numerical tests for various configurations of piezoelectric materials, it is found that depending on the choice of penalization value, complex behaviors of energies are possible and these in turn lead to a serious local optima issue in TO. Through several three-dimensional design problems, the validity and usefulness of the developed optimization procedure for efficient EHDs are demonstrated.

1. Introduction

This study develops a finite element procedure for topology optimization (TO) scheme for the optimal design of piezoelectric energy harvesting devices (EHDs) by considering the static and harmonic dynamic responses of piezoelectric EHDs; among many energy harvesting sources such as ambient-radiation, biomechanical energy, photovoltatic, pyroelectric energy, and magnetostatic, we only consider the piezoelectric energy harvesting devices. Over the last few decades, the design of eco-friendly and optimal energy or power harvesting devices that generate electric energy from otherwise untapped and inexhaustible sources such as sunlight, wind, vibrating machines, and acoustic pressure has gained considerable importance [1,2,4–11]. As commonly simple geometries such as circle, triangular and rectangular shape structures have been used, much improvement can be done by topological optimization [4–11]. This paper presents a TO scheme for the design of efficient piezoelectric EHDs [12]. TO could be advantageous in an electro-mechanical coupling system because it can provide optimal topologies for piezoelectric EHDs by minimizing or maximizing a given objective function subject to some engineering constraints [4–11,13–16].

Piezoelectric materials have attracted considerable academic and industrial interest because their piezoelectricity and reverse piezoelectricity can be easily exploited to manufacture mechanical actuators and sensors. Piezoelectric materials exhibit such properties because of the change in the polarization direction within the material volume, as illustrated by the Heckmann diagram in Fig. 1 [1,2]. Furthermore, various methods have been developed for manufacturing electromechanical coupling systems that can be applied to efficient EHDs or active compliant actuators. Zheng et al. [3] optimized the layouts of EHDs by considering the static load. Rupp et al. [5] studied a dynamic piezoelectric EHD for plate structures. Dono et al. [9,10] studies the piezoelectric bimorph shell actuators for static and dynamic load. Silva and Kikuchi [6], Silva et al. [7,8], Canfield and Frecker [15], Carbonari et al. [18], Silva et al. [19], Carbonari et al. [17], and Kim et al. [20] studied optimal topologies for compliant mechanisms and sensors realized using piezoelectric materials. Kang and Tong [14] studied the optimal design of an electrode using TO. Recently, Luo et al. [21] and Chen et al. [22] studied levelset-based TO for piezoelectric materials. To the best of our knowledge, among all the recent studies mentioned above, only Rupp et al. considered the dynamic load effect (see [5] and references therein). Here, it is noteworthy that the electric energy generated by a *static* mechanical load with a closed circuit is released rapidly. For a continuous EHD, an oscillating mechanical force should be applied. Therefore, as an extension of the

* Corresponding author.
E-mail addresses: ghy@hanyang.ac.kr, gilho.yoon@gmail.com (G.H. Yoon).

0965-9978/$ - see front matter © 2012 Elsevier Ltd. All rights reserved.
http://dx.doi.org/10.1016/j.advengsoft.2012.07.008

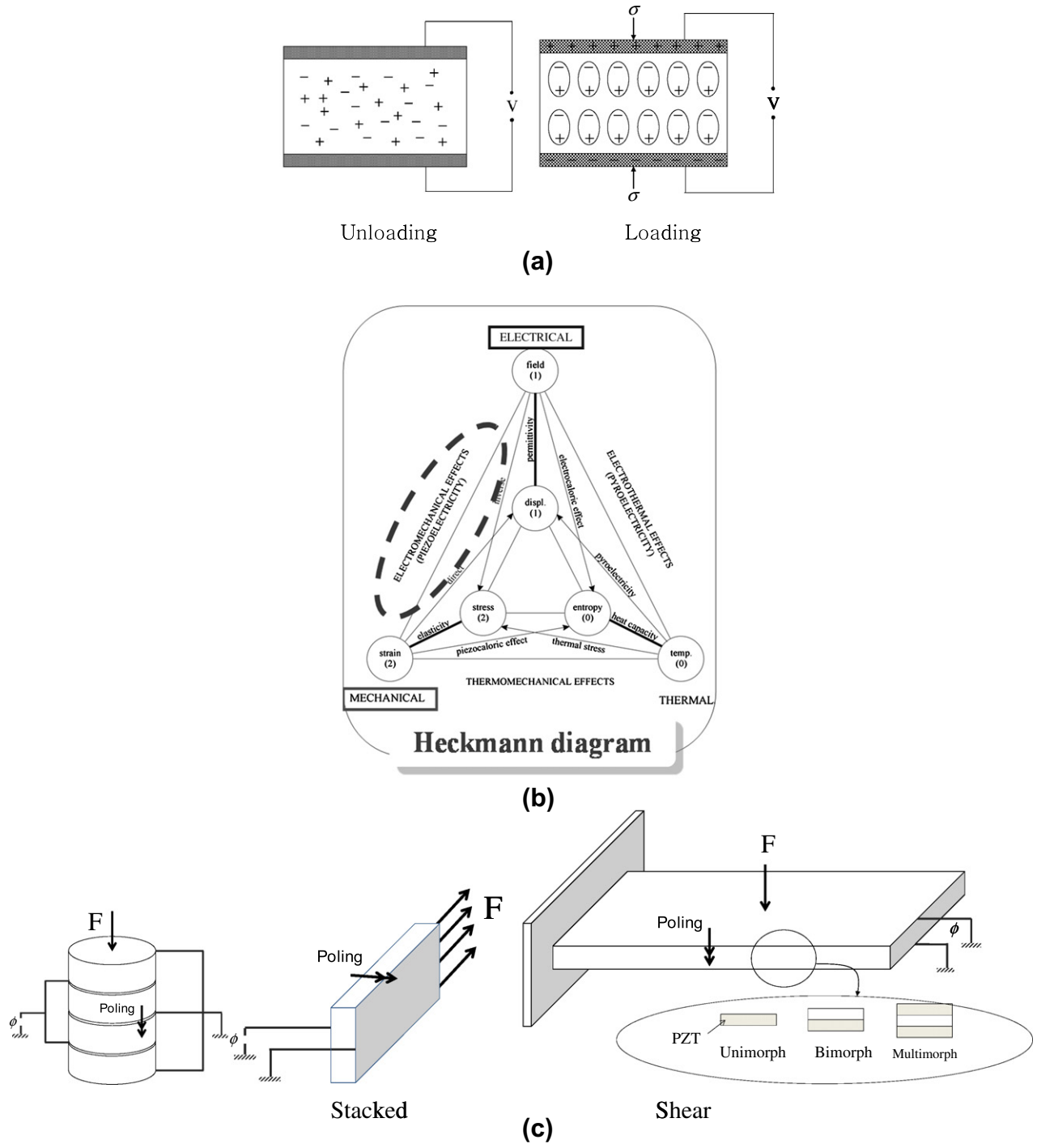

Fig. 1. (a) Piezoelectric phenomenon, (b) Heckmann diagram [2], and (c) typical piezoelectric energy harvesting devices (EHDs). (The double arrows are used to represent the poling direction throughout this paper.)

abovementioned studies, this study focuses on the application of TO to optimal EHDs by developing an in-house FE code that considers static and dynamic loads. It is possible to adopt the commercial CAE software such as Nastran or ANSYS for analysis. Nevertheless, because the internal information of FEM such as element stiffness matrix, strain–displacement matrix is necessary for the efficient sensitivity analysis, it was better to develop an in-house FE code in this research.

This study considers the effect of static and the effect of harmonic dynamic loads (hereafter, the dynamic piezoelectric effect) on TO for the optimal design of an EHD based on the solid isotropic material with penalization (SIMP) approach; to our best knowledge, commonly the static or the harmonic dynamic loads are applied to an EHD and some EHD devices for wind movement, human movement or shock that are not harmonic dynamic loads can be engineered in consideration of frequency response model. For an example of harmonic dynamic loads, we can list the fluid force from wave, the vibration energy from an engine or similar structures. To the best of our knowledge, few studies on TO have considered dynamic piezoelectric effects [5–8]. Most studies have considered the static TO problem by interpolating the stiffness matrix (and not Young's modulus), piezoelectricity matrix, and

permittivity matrix of each PZT element with respect to an element density design variable. As mentioned in the previous paragraph, for a continuous electric EHD, an oscillating mechanical force should be applied to compensate the released electric energy. Indeed, this paper focuses on the development of a topology optimization method for maximizing the energy harvesting efficiency by harmonic dynamic loads. Toward this end, various aspects of a piezoelectric material and the optimization formulations of energies with complex responses are studied.

The remainder of this paper is organized as follows. Section 2 introduces the theory and FE formulation of piezoelectric materials. Sections 3 and 4 present several optimization formulations to improve the efficiencies of EHDs, optimization results, and some physical interpretations of the obtained designs, along with the effect of the penalization values on the optimized results. Finally, Section 5 summarizes the findings and discusses possible future works.

2. Finite element formulation for piezoelectric material

2.1. Static FE formulation

The performance and efficiency of an EHD for general mechanical and electric boundary configurations can be easily and accurately analyzed by an FE procedure. To simplify the computation, the piezoelectric material is assumed to have linear material properties. Then, the electromechanical coupling phenomena between mechanical and electrical domains are formulated as follows [1,2]:

$$\mathbf{T} = \mathbf{c}^{\mathbf{E}}\mathbf{S} - \mathbf{e}\mathbf{E} \tag{1}$$

$$\mathbf{D} = \mathbf{e}^{\mathbf{T}}\mathbf{S} + \boldsymbol{\varepsilon}^{\mathbf{S}}\mathbf{E} \tag{2}$$

where the mechanical stress and strain are denoted by $\mathbf{T}$ and $\mathbf{S}$, respectively. The so-called electric displacement and electric field are denoted by $\mathbf{D}$ and $\mathbf{E}$, respectively. For FE simulations of the piezoelectric material, the linear stiffness matrix $\mathbf{c}^{\mathbf{E}}$ (also called the stiffness tensor), piezoelectric matrix $\mathbf{e}$, and permittivity matrix $\boldsymbol{\varepsilon}^{\mathbf{S}}$ are used. Unless stated otherwise, we only use a PZT-4 material polarized along the Y-direction in Cartesian coordinates for all the analyses and numerical examples reported herein (see Section 4 for more details).

Without loss of generality, the FE procedure with the standard linear 8-node brick element is developed with the displacements ($\mathbf{u}$) and potential ($\boldsymbol{\varphi}$) as the primary (unknown) FE variables. The resulting FE equations of the eth PZT element can be written as follows [23–27]:

$$\begin{bmatrix} \mathbf{K}^e_{\mathbf{uu}} & \mathbf{K}^e_{\mathbf{u}\varphi} \\ \mathbf{K}^e_{\varphi\mathbf{u}} & -\mathbf{K}^e_{\varphi\varphi} \end{bmatrix} \begin{bmatrix} \mathbf{u}^e \\ \varphi^e \end{bmatrix} = \begin{bmatrix} \mathbf{F}^e \\ \mathbf{Q}^e \end{bmatrix} \tag{3}$$

where the mechanical loads and electric charges of the eth element are denoted by $\mathbf{F}^e$ and $\mathbf{Q}^e$, respectively. The mechanical displacements and potentials of the eth element having the element domain Ω_e are denoted by $\mathbf{u}^e$ and $\boldsymbol{\varphi}^e$, respectively. The structural stiffness matrix, piezoelectric matrix, and electric matrix of the eth element are denoted by $\mathbf{K}^e_{\mathbf{uu}}$, $\mathbf{K}^e_{\mathbf{u}\varphi}(\mathbf{K}^e_{\varphi\mathbf{u}})$, and $\mathbf{K}^e_{\varphi\varphi}$, respectively, and these FE matrices are formulated as

$$\begin{aligned} \mathbf{K}^e_{\mathbf{uu}} &= \int_{\Omega_e} \mathbf{B}^{\mathbf{T}}_{\mathbf{u}}\mathbf{c}^{\mathbf{E}}\mathbf{B}_{\mathbf{u}}\,dv, \quad \mathbf{K}^e_{\mathbf{u}\varphi} = \int_{\Omega_e} \mathbf{B}^{\mathbf{T}}_{\mathbf{u}}\mathbf{e}\mathbf{B}_{\varphi}\,dv \\ \mathbf{K}^e_{\varphi\mathbf{u}} &= \int_{\Omega_e} \mathbf{B}^{\mathbf{T}}_{\varphi}\mathbf{e}^{\mathbf{T}}\mathbf{B}_{\mathbf{u}}\,dv, \quad \mathbf{K}^e_{\varphi\varphi} = \int_{\Omega_e} \mathbf{B}^{\mathbf{T}}_{\varphi}\boldsymbol{\varepsilon}^{\mathbf{S}}\mathbf{B}_{\varphi}\,dv \end{aligned} \tag{4}$$

where the strain–displacement transformation matrix for $\mathbf{u}^e$ and the electric field–potential transformation matrix for $\boldsymbol{\varphi}^e$ are denoted by $\mathbf{B}_{\mathbf{u}}$ and $\mathbf{B}_{\boldsymbol{\varphi}}$, respectively. For an EHD system, the sets of linear equations can be assembled as follows [23–27]:

$$\begin{bmatrix} \mathbf{K}_{\mathbf{uu}} & \mathbf{K}_{\mathbf{u}\varphi} \\ \mathbf{K}_{\varphi\mathbf{u}} & -\mathbf{K}_{\varphi\varphi} \end{bmatrix} \begin{bmatrix} \mathbf{u} \\ \boldsymbol{\varphi} \end{bmatrix} = \begin{bmatrix} \mathbf{F}_t \\ \mathbf{Q}_t \end{bmatrix} \tag{5}$$

$$\begin{aligned} \mathbf{K}_{\mathbf{uu}} &= \sum_{e=1}^{NE} \mathbf{K}^e_{\mathbf{uu}}, \quad \mathbf{K}_{\mathbf{u}\varphi} = \sum_{e=1}^{NE} \mathbf{K}^e_{\mathbf{u}\varphi} \\ \mathbf{K}_{\varphi\mathbf{u}} &= \sum_{e=1}^{NE} \mathbf{K}^e_{\varphi\mathbf{u}}, \quad \mathbf{K}_{\varphi\varphi} = \sum_{e=1}^{NE} \mathbf{K}^e_{\varphi\varphi} \end{aligned} \tag{6}$$

where the total number of PZT elements is NE. The global stiffness matrices are $\mathbf{K}_{\mathbf{uu}}$, $\mathbf{K}_{\mathbf{u}\varphi}(\mathbf{K}_{\varphi\mathbf{u}})$, and $\mathbf{K}_{\varphi\varphi}$, and the global vectors for the structural displacements and potential are $\mathbf{u}$ and $\boldsymbol{\varphi}$, respectively. To solve the above set of linear equations, appropriate boundary conditions for the structural and electric displacements are assumed to be enforced. For the non-homogeneous boundary condition for electrodes, i.e., non-zero electric potential on some sections of the boundary domains, the penalization formulation is employed and it results in a non-symmetric stiffness matrix. This non-symmetric stiffness matrix feature is considered when deriving the sensitivity values of an objective function with respect to design variables in the subsequent section (see Appendix A). Furthermore, the equipotentiality in electric electrodes is also enforced by assigning single degrees of freedom for the voltage within the electric electrodes [28]. Mathematically, the following modified stiffness matrices can be used:

$$\tilde{\boldsymbol{\varphi}} = \mathbf{M}_{EQ}\boldsymbol{\varphi} \tag{7}$$

$$\widetilde{\mathbf{K}}_{\varphi\varphi} = \mathbf{M}^{\mathbf{T}}_{EQ}\mathbf{K}_{\varphi\varphi}\mathbf{M}_{EQ}, \quad \widetilde{\mathbf{K}}_{\mathbf{u}\varphi} = \mathbf{K}_{\mathbf{u}\varphi}\mathbf{M}_{EQ}, \quad \widetilde{\mathbf{K}}_{\varphi\mathbf{u}} = \mathbf{M}^{\mathbf{T}}_{EQ}\mathbf{K}_{\varphi\mathbf{u}} \tag{8}$$

where the electric potential for the equipotentiality is $\tilde{\boldsymbol{\varphi}}$ and the matrix $\mathbf{M}_{EQ}$ imposes this equipotentiality condition on $\boldsymbol{\varphi}$ (see [23,28] for the detail implementation). The modified matrices have tilt notations. The developed FE code is verified using commercially available ANSYS software.

2.2. Harmonic dynamic FE formulation and circuit model

To describe the motion of the piezoelectric material by means of a set of independent generalized coordinates, the Lagrange equation of motion can be applied by considering the mutual coupling effects of the electric and mechanical systems. To formulate the harmonic dynamic equation in the framework of FEM, the time-harmonic response due to the time-harmonic excitation is calculated [26,27]. The coupled governing equations describing between the time varying structural displacements ($\mathbf{u}_t$) and the time varying potential $\boldsymbol{\varphi}_t$ are given as follows:

$$\begin{bmatrix} \mathbf{M} & \mathbf{0} \\ \mathbf{0} & \mathbf{0} \end{bmatrix} \begin{bmatrix} \ddot{\mathbf{u}}_t \\ \ddot{\boldsymbol{\varphi}}_t \end{bmatrix} + \mathbf{C} \begin{bmatrix} \dot{\mathbf{u}}_t \\ \dot{\boldsymbol{\varphi}}_t \end{bmatrix} + \begin{bmatrix} \mathbf{K}_{\mathbf{uu}} & \mathbf{K}_{\mathbf{u}\varphi} \\ \mathbf{K}_{\varphi\mathbf{u}} & \mathbf{K}_{\varphi\varphi} \end{bmatrix} \begin{bmatrix} \mathbf{u}_t \\ \boldsymbol{\varphi}_t \end{bmatrix} = \begin{bmatrix} \mathbf{F}_t \\ \mathbf{Q}_t \end{bmatrix} \tag{9}$$

By assuming the time-harmonic response due to the time-harmonic excitations$[\mathbf{F}_t\mathbf{Q}_t] = [\mathbf{F}\mathbf{Q}]e^{i\omega t}$, the coupled governing equations in frequency domain are obtained as follows:

$$\left\{ -\omega^2 \begin{bmatrix} \mathbf{M} & \mathbf{0} \\ \mathbf{0} & \mathbf{0} \end{bmatrix} + i\omega\mathbf{C} + \begin{bmatrix} \mathbf{K}_{\mathbf{uu}} & \mathbf{K}_{\mathbf{u}\varphi} \\ \mathbf{K}_{\varphi\mathbf{u}} & -\mathbf{K}_{\varphi\varphi} \end{bmatrix} \right\} \begin{bmatrix} \mathbf{u} \\ \boldsymbol{\varphi} \end{bmatrix} = \begin{bmatrix} \mathbf{F} \\ \mathbf{Q} \end{bmatrix} \tag{10}$$

$$\mathbf{M} = \sum_{e=1}^{NE} \mathbf{m}^e_{\mathbf{uu}}, \quad \mathbf{m}^e_{\mathbf{uu}} = \int_{\Omega_e} \rho\mathbf{H}^{\mathbf{T}}_{\mathbf{u}}\mathbf{H}_{\mathbf{u}}\,dv, \quad \mathbf{C} = \alpha \begin{bmatrix} \mathbf{M} & \mathbf{0} \\ \mathbf{0} & \mathbf{0} \end{bmatrix} + \beta \begin{bmatrix} \mathbf{K}_{\mathbf{uu}} & \mathbf{K}_{\mathbf{u}\varphi} \\ \mathbf{K}_{\varphi\mathbf{u}} & \mathbf{K}_{\varphi\varphi} \end{bmatrix} \tag{11}$$

the excitation angular speed is denoted by ω and the coefficients of Rayleigh damping are α and β. The mass matrix and the shape function of the eth element are $\mathbf{m}^e_{\mathbf{uu}}$ and $\mathbf{H}_{\mathbf{u}}$, respectively. The density of the piezoelectric material is denoted by ρ.

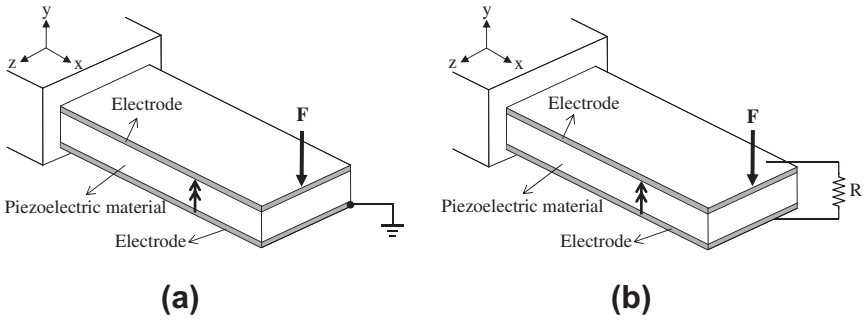

Fig. 2. FE models (a) without a resistor and (b) with a resistor [30].

Furthermore, the developed FE code can be used to simulate the dynamic behavior of a piezoelectric system connected to an electric circuit [29,30]. For example, to simulate an EHD system connected to a closed electric circuit (Fig. 2b), say, a typical electric device such as a pump or motor, Eq. (9) can be modified to Eq. (12). To focus on the design of the EHD, only a resistor having a positive real valued magnitude is simulated. However, a complex value enables the analysis of the dynamic response with a complex electric circuit.

With *NR* resistors, the above Eq. (9) is reformulated as follows:

$$\left\{-\omega^2\begin{bmatrix}\mathbf{M} & \mathbf{0}\\ \mathbf{0} & \mathbf{0}\end{bmatrix}+i\omega\mathbf{C}+\begin{bmatrix}\mathbf{K}_{\mathbf{uu}} & \mathbf{K}_{\mathbf{u}\varphi}\\ \mathbf{K}_{\varphi\mathbf{u}} & -\mathbf{K}_{\varphi\varphi}\end{bmatrix}-\frac{i}{\omega}\sum_{j=1}^{NR}\frac{1}{R_j}\right\}\begin{bmatrix}\mathbf{u}\\ \boldsymbol{\varphi}\end{bmatrix}=\begin{bmatrix}\mathbf{F}\\ \mathbf{Q}\end{bmatrix} \tag{12}$$

where the total number of resistors used is *NR*. For the sake of simplicity, we denote the assembly of the resistors as the summation. From the above equation, the following observations can be made.

1. A resistor with a positive valued magnitude acts as a nonlinear damping.
2. Even without Rayleigh damping (structural damping), complex equations can be solved with a resistor and the complex sensitivity analysis can be derived for associated complex objective functions such as the electric energy, strain energy, or conversion factor (ratio of electric energy to total potential energy).

3. Material interpolation and topology optimization

3.1. Interpolation functions for topological optimization

One of the difficulties involved in TO is that an optimization problem with a discrete design variable (zero or one) should be solved to determine solid domains (solid) or non-solid domains (void) [12,16]. To cope with this difficulty, we usually introduce a continuous design variable to relax the optimization problem with a discrete design variable into an optimization problem with a continuous design variable varying from zero to one using simple polynomial functions. For example, it is known that we can use a polynomial function with a power of 3 or 4, which is known as the solid isotropic material with penalization (SIMP) method, to interpolate Young's modulus with respect to the density design variable for the compliance minimization problem [12,16]. To apply the SIMP-based interpolation function to a piezoelectric material, the following interpolation formulation can be adopted without loss of generality.

$$\begin{bmatrix}(\gamma_e)^{p_1}\mathbf{K}^e_{\mathbf{uu}} & (\gamma_e)^{p_2}\mathbf{K}^e_{\mathbf{u}\varphi}\\ (\gamma_e)^{p_2}\mathbf{K}^e_{\varphi\mathbf{u}} & -(\gamma_e)^{p_3}\mathbf{K}^e_{\varphi\varphi}\end{bmatrix}\quad(0<\gamma_e\leqslant 1) \tag{13}$$

where the penalization values for the structural stiffness, piezoelectric, and permittivity matrices are p_1, p_2, and p_3, respectively. Note that some combinations of different penalization values can be used with the density design variable of the eth element (γ_e).

For the interpolation of the mass matrix, the following linear interpolation function is employed [12,13].

$$\gamma_e\mathbf{M}^e_{\mathbf{uu}} \tag{14}$$

Numerical tests presented below suggest that the penalization values employed in (13) and (14) strongly affect the design of the optimal layout for the piezoelectric material. Although there are other material interpolations such as RAMP, we confine ourselves to the linear approach of (14) in order to show the effects of the penalty parameters of (13) [12]. The following remarks can be made.

Remark 1. Depending on the penalization values of p_1, p_2, and p_3, very different layouts are obtained. This appears to be attributable to the local optima issue as well as the different physical behavior issue depending on the employed penalization values.

Remark 2. A higher penalization value occasionally does not guarantee an optimal layout with distinct solid-void design variables. Different combinations among p_1, p_2, and p_3 should be studied.

First, previous studies have not clearly described the effects of these penalization values on a dynamic system. In this study, several numerical tests were performed, the results of some of which are presented in the subsequent sections, and very different designs were obtained. Using some combinations of these penalization parameters, some optimal layouts with many grey elements and disconnected domain designs can be obtained even with a higher penalization value such as 3 or 4. Furthermore, some combinations of penalization values that provide physically acceptable layouts for some loading and boundary conditions do provide unrealistic layouts with different loading and boundary conditions. After investigating the optimal layouts with many combinations, it is found that these interesting phenomena are attributable to the different physical behaviors among the electric matrix, coupling matrix, and structural matrix. Second, we know that at least in the compliance minimization problem, higher penalizations to Young's modulus tend to lead to optimal layouts that clearly converge to either solid or void. However, in this EHD system, several combinations with higher penalization values occasionally do not guarantee optimal layouts that clearly converge either to solid or void. Additionally, the employed interpolation functions do not interpolate physics; the design domains simulated by a lower bound are non-structural domains and not domains for other physics [31].

3.2. Objective function and sensitivity analysis

3.2.1. Energy conversion factor and electromechanical coupling coefficient (EMCC)

Some previous studies on EHD have been based on the electromechanical coupling coefficient (EMCC) or the conversion factor (see [4,32,33] for more details). Although the details of their formulations are different, it appears that the overall meanings are the same at least for a static EHD system. Thus, only the energy conversion factor is discussed herein.

$$\eta = \frac{\prod_{ab}(\omega) - \prod_{ca}(\omega)}{\prod_{ab}(\omega)} = \frac{\Pi_E(\omega)}{\Pi_S(\omega) + \Pi_E(\omega)} \tag{15}$$

To evaluate the EMCC for a piezoelectric EHD and the effectiveness of the energy conversion from mechanical energy to electric energy and vice versa, an experiment based on a closed-loop quasi-static energy cycle, as shown in Fig. 3a, can be employed. For the first stage, an external mechanical load is applied to a piezoelectric material for the reverse piezoelectric effect in the open-circuit condition (without external circuit) from (a) to (b) in Fig. 3a. From the principle of energy conservation, the externally applied mechanical energy is clearly converted to the internal mechanical and electric energies stored in the piezoelectric material. By adding a resistor, whose magnitude can be complex for an equivalent resistor consisting of a resistor, inductor, and capacitor, the stored electric energy at state (b) is released. From state (c), the piezoelectric body returns to the original configuration because of the stored elastic energy from (c) to (a) without the external mechanical load. By repeating these steps, otherwise untapped electric energy can be harvested from the external load. Hence, the dissipated electric energy in the resistor clearly originates from the electric energy in state (b). Furthermore, it should be emphasized that the quasi-static energy cycle is assumed here. However, as stated in the previous section, to harvest electric energy continuously, a dynamic load should be applied, as shown in Fig. 3b. Therefore, the internal mechanical and electric energies used to calculate the energy conversion factor should be dependent on an excitation angular velocity because of the consideration of the dynamic effect. To the best of our knowledge, some studies have used this EMCC as an index or objective in the structural optimization of piezoelectric EHDs [6]. However, because the present study considers a dynamic load rather than a specific resonating mode, other formulations presented in the subsequent sections are used by calculating these dynamic energies directly (see Appendix A to see the effects of structural resonances and electrical resonances and B to see the effects of the formation of piezoelectric material on EHDs).

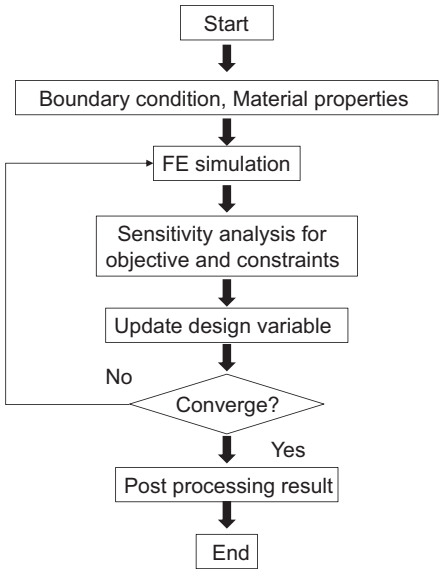

Fig. 4. Topology design optimization procedure.

With the developed finite element code and the sensitivity analysis (Appendix C), the optimization procedure shown in Fig. 4 is implemented with the method of moving asymptotes (MMA) [34] for an optimization algorithm.

3.3. Analysis example with different penalization values

3.3.1. Influences of combinations of penalization values

To illustrate the effects of the penalization values in (13), the one element problem with a point load is considered in Fig. 5a. For the FE boundary condition, the 4 nodes of the side of the element are clamped and a point load is applied at one of the nodes located at the top side. To simulate the top and bottom electrodes, the four degrees of freedom of the voltage of the top and bottom layers are merged.

First, Fig. 5b shows the curves of the conversion factors with several different combinations of the penalization values by varying the density design variable from 0 to 1. It is interesting to note

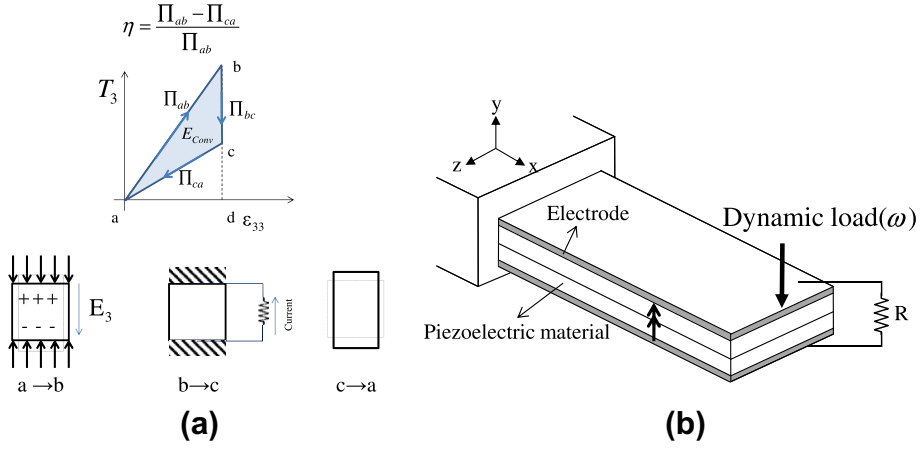

Fig. 3. (a) Closed-loop quasi-static energy cycle for a piezoelectric body to calculate EMCC and the conversion factor [33] and (b) concept of dynamic electromechanical system.

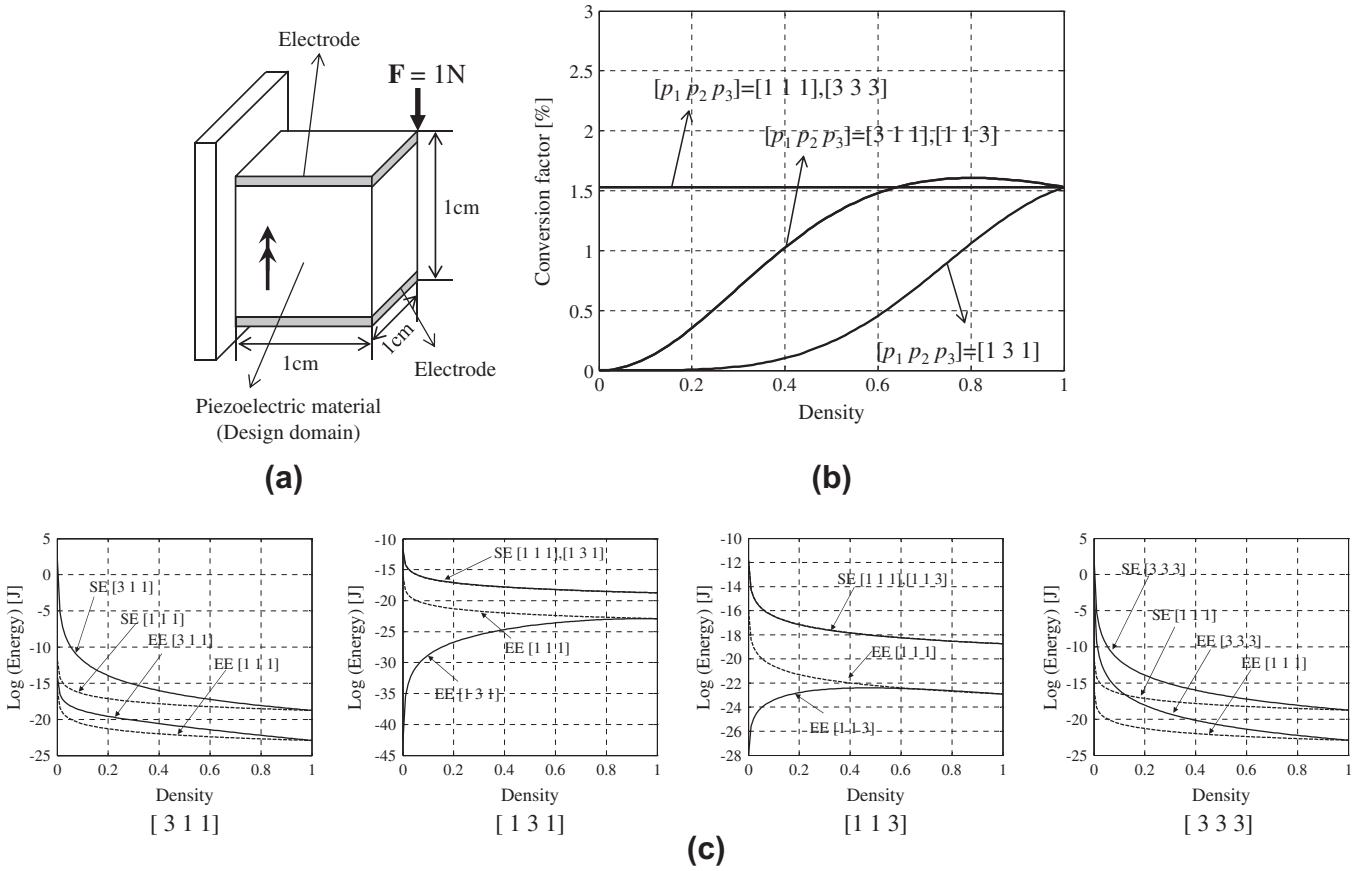

Fig. 5. An illustrative example (mesh $1 \times 1 \times 1$) (SE: static energy, EE: electric energy). (a) A model (a PZT-4 material polarized along the Y-direction in Cartesian coordinates), (b) conversion factor curves with different penalization values, and (c) curves of energies.

that the curves of the conversion factor for the same penalization values, i.e., [1 1 1] or [3 3 3] for p_1, p_2, and p_3 become constant with respect to the design variable, implying that the density design variable does not affect the conversion factor; hereafter, the values in the square bracket represent the respective employed penalization values. Furthermore, with [3 1 1] and [1 1 3], identical curves are obtained, as shown in Fig. 5b. To investigate these cases further, Fig. 5c shows the electric and elastic energy curves with different penalization values with the curve of [1 1 1] shown as a reference. As shown, very different behaviors of the energies are observed. Indeed, it can be postulated that different penalization values lead to different physics interpolations and different topological layouts.

4. Synthesis of energy harvesting device

To validate the usefulness and performance of the developed optimization theory, the layouts of three-dimensional EHDs are optimized. We start with an optimization problem by considering an energy conversion factor subject to a mass constraint for static loads. Numerical tests with different penalization values suggest that the optimization formulation using the energy conversion factor has some drawbacks on account of local optima and disconnected designs. To resolve these side-effects, we propose an alternative formulation subject to a static compliance constraint. Furthermore, we extend our consideration to dynamic loads. In all the presented numerical examples, three-dimensional regular meshes and the PZT-4 material formulated by (16)–(18) are used. The geometry and boundary conditions are chosen so as to show the potential application of the abovementioned theory to TO for EHDs. In addition, the sensitivity filter with 1.5 times of the element size radius is applied to the sensitivity values of an objective and constraints. For the stopping criterion, the maximum iteration is set to 300 and the relative differences of the design variables and the objective function values are considered. Also the mesh independent sensitivity filter is employed [12]. As stated in Section 2, the PZT-4 material is only considered for all the examples. The implemented matrices of the material properties of the PZT-4 material can be rewritten as follows:

$$\mathbf{e} = \begin{bmatrix} 0 & -5.2 & 0 \\ 0 & 15.1 & 0 \\ 0 & -5.2 & 0 \\ 12.7 & 0 & 0 \\ 0 & 0 & 12.7 \\ 0 & 0 & 0 \end{bmatrix} \text{C/m}^2 \quad (\text{polarized along the } Y\text{-direction}) \tag{16}$$

$$\boldsymbol{\varepsilon}^{\mathbf{S}} = \begin{bmatrix} 730 & 0 & 0 \\ 0 & 635 & 0 \\ 0 & 0 & 730 \end{bmatrix} \times \varepsilon_{air} \quad (\varepsilon_{air}: \text{ the permittivity of air}) \tag{17}$$

$$\mathbf{c}^{\mathrm{E}} = \begin{bmatrix} 13.9 & 7.43 & 7.78 & 0 & 0 & 0 \\ 7.43 & 11.5 & 7.43 & 0 & 0 & 0 \\ 7.78 & 7.43 & 13.9 & 0 & 0 & 0 \\ 0 & 0 & 0 & 2.56 & 0 & 0 \\ 0 & 0 & 0 & 0 & 2.56 & 0 \\ 0 & 0 & 0 & 0 & 0 & 3.06 \end{bmatrix} 10^{10}\ \text{N/m}^2 \tag{18}$$

Note that matrices (16)–(18) are written for FE formulations for Cartesian coordinates.

4.1. Example 1: Maximizing energy conversion factor for a static point load

First, the optimal piezoelectric material distribution of a unimorph EHD for an end point load is considered in Fig. 6. In this example, the entire PZT substrate is set to a design domain and the upper and electrical ground bottom electrodes are modeled using Eqs. (7) and (8). In other words, to maximize the efficiency of this unimorph EHD, we can distribute the piezoelectric materials within the design domain. The design domain (2 cm × 4 cm × 0.2 cm) is discretized by 1600 brick elements (8 nodes) and the design variables of the top and bottom layers are linked along the *Y*-direction to prevent a complex manifold structure after optimization; the basic parameters and the geometries in [4] are employed. The objective of this first numerical example is to maximize the conversion factor subject to the mass constraint where the usage of the piezoelectric material is limited to up to 60% proposed in [4].

$$\begin{aligned} &\text{Max} \quad \eta \\ &\text{s.t.} \quad \sum_{e=1}^{NED} \gamma_e v_e \leqslant V^* \end{aligned} \tag{19}$$

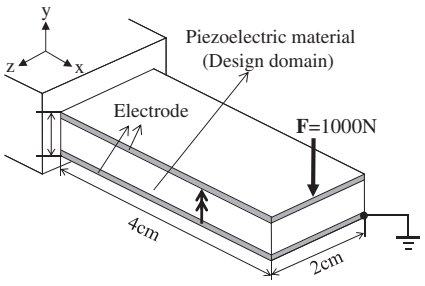

Fig. 6. Problem definition for topology optimization with a point load (V^*: 60%).

where *NED* is the number of FE elements in the design domain. The volume constraint is denoted by V^* and is set to 60% of the entire design domain.

Using some combinations of penalization values (without a continuous approach for penalizations), the optimal layouts shown in Fig. 7 can be obtained with an evenly distributed initial density satisfying the mass constraint. As an illustrative example, the top views of the material distributions are plotted. Because many possible combinations for the penalization values exist, several different combinations of the penalization values [p_1, p_2, p_3] are tested in Fig. 7. As shown in the figure, the various layouts whose topologies differ considerably from each other can be obtained depending on the employed penalization values. We cannot treat these different layouts as the simple local optima issue of TO, as discussed in Section 3.3. Furthermore, to show the effects of the implicit penalties of the SIMP method, we intentionally use a lower penalization, 1, for the penalization value of the compliance matrix in some examples. From these obtained layouts, some important observations can be made. First, in addition to the intermediate design variable issue rendering the associated elements as gray, the disconnected regions, which are impossible to manufacture and are physically unacceptable, are obtained by maximizing the energy conversion factors with [1 1 1] and [3 1 1]; the design with [3 3 3] is not a clearly disconnected design. The investigation of figure (b) reveals that because the energy conversion factor is defined as the ratio of the electric energy to the summation of the electric and strain energies, we can often obtain such disconnected designs having larger conversion factors. For examples, with the penalization combinations of [1 1 1], [3 1 1], and [3 3 3], the static compliances are very high because of the disconnected domains; however, the electric energies are also high. Second, although this has not been presented, changing the characteristics of the problem, such as the boundary condition, electrode condition, or penalization value combination (i.e., [1 3 1] or [1 1 3]), does not eliminate disconnected designs having higher structural compliances. Furthermore, it is also recognized that it becomes problematic to quantitatively measure and calculate the energies by maximizing the energy conversion factor.

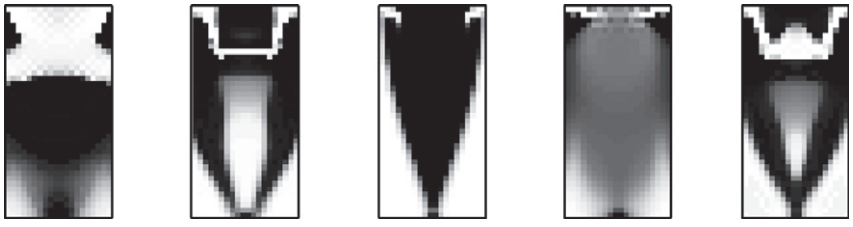

[1 1 1] [3 1 1] [1 3 1] [1 1 3] [333]

(a)

[$p_1p_2p_3$]	[1 1 1] (Physically not acceptable)	[3 1 1] (Physically not acceptable)	[1 3 1]	[1 1 3]	[3 3 3] (Physically not acceptable)
Static strain energy (J)	109.5866	37.6405	9.5067	12.3808	1955.0496
Static electric energy (J)	12.4341	158.9877	0.6240	1.3268	463.8975
Conversion factor (%)	10.1901	80.8570	6.1594	9.6793	19.1776

(b)

Fig. 7. Optimization results with different penalization values.

From the observations of these numerical tests and the highly nonlinear curves of the objective function, it is likely that only a fortune can resolve these local optima issue with disconnected domains using the optimization formulation (19).

Furthermore, we compare the layouts that minimize the static compliance with one of the above designs. As shown in Fig. 8, with some combinations of penalization values, a layout similar to that which minimizes the static compliance with small differences can be obtained.

4.2. Example 2: Maximizing electric energy subject to static strain energy for a static point load

As shown in the first numerical example, we experience some side-effects of the optimization formulation when maximizing the energy conversion factor. To prevent these side-effects and to maximize the electric energy itself, we propose the following formulation for TO of EHDs with static loads; the finite element meshes and the employed material properties of the following numerical examples (Examples 2–4) unless otherwise stated are same as those of the first numerical example.

$$\begin{aligned} \text{Max} \quad & \Phi = \prod_{E} (\text{static electric energy}) \\ \text{s.t.} \quad & \sum_{e=1}^{NED} \gamma_e v_e \leqslant V^* (V^* : \ 60\%) \\ & \prod_{S} \leqslant \prod_{S}^{*} \left(\prod_{S}^{*} : \ \text{The upper bound of the static strain energy} \right) \end{aligned} \tag{20}$$

where the strain energy of the considered system and the upper bound of the static strain energy are denoted by $\prod_S$ and $\prod_S^*$, respectively. In this present formulation, we directly maximize the electric energy and impose an additional constraint for the static strain energy because we want to maximize the stored electric energy. By controlling the upper bound of the strain energy, we expect that it is possible to control the compliance of the structure and with an appropriate value of $\prod_S^*$ from an engineering viewpoint, it is expected that disconnected design regions can be eliminated. To verify this hypothesis, the penalization values of [1 3 1] and [3 1 1] are tested using the optimization formulation (20) in Figs. 9 and 10. With this optimization formulation, it is possible to obtain connected domains with larger electric energies and larger conversion

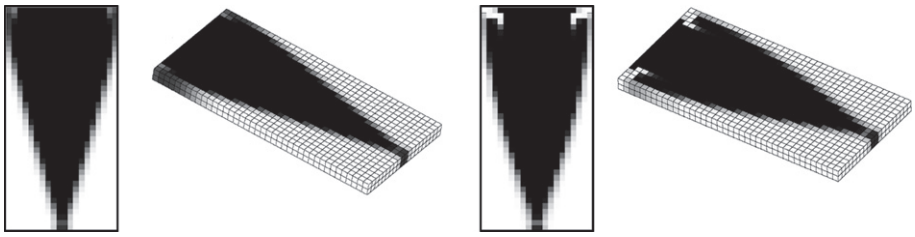

Conversion factor: 5.4366% Conversion factor: 6.1595%

(a) (b)

Fig. 8. Comparison between (a) layout minimizing the mechanical compliance (strain energy: 9.2223 J, electric energy: 0.5302 J) and (b) layout maximizing the conversion factor (strain energy: 9.5067 J, electric energy: 0.6204 J, penalization values: [1 3 1]).

$\prod_S^* = 10$ J $\prod_S^* = 11$ J $\prod_S^* = 12$ J $\prod_S^* = 13$ J

Strain energy (J)	9.9590
Electric energy (J)	0.6653
Conversion factor (%)	6.2624

Strain energy (J)	11.0092
Electric energy (J)	0.7638
Conversion factor (%)	6.4882

Strain energy (J)	12.0077
Electric energy (J)	0.8084
Conversion factor (%)	6.3083

Strain energy (J)	13.0060
Electric energy (J)	0.8539
Conversion factor (%)	6.1612

Fig. 9. Optimization results with strain energy constraint using penalization values of [1 3 1].

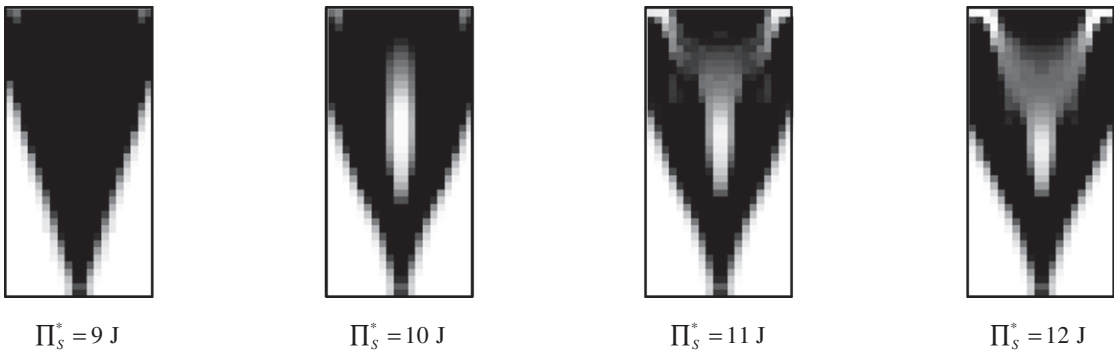

Strain energy (J)	9.0609
Electric energy (J)	0.5589
Conversion factor (%)	5.8102

Strain energy (J)	10.0017
Electric energy (J)	0.5935
Conversion factor (%)	5.6019

Strain energy (J)	10.9932
Electric energy (J)	1.0080
Conversion factor (%)	8.3994

Strain energy (J)	12.0214
Electric energy (J)	1.6577
Conversion factor (%)	12.1186

Fig. 10. Optimization results with strain energy constraint using penalization values of [3 1 1].

factors in Figs. 9 and 10. Note that with the lower upper bound compliance, i.e., 10 J with [1 3 1], it is possible to recover the design shown in Figs. 7 and 9. It is recognized that the conversion factor of the first design with $\prod_S^* = 10$ J in Fig. 9 is larger as compared to that of the design in Fig. 7. Furthermore, in our opinion, it is advantageous that the compliance can be controlled and the electric energy can be maximized independently.

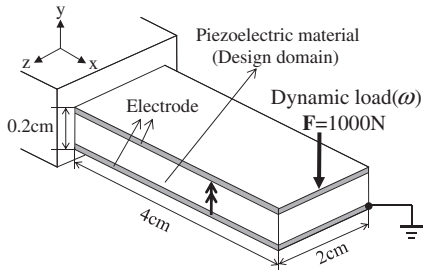

Fig. 11. Problem definition with a dynamic point load.

4.3. Example 3: Maximizing electric energy subject to static strain energy for a dynamic point load

Thus far, we have considered the TO of EHDs for static loads that is the main subject of the research paper [4,20]. As shown in the previous numerical examples, we obtain the similar results and the same conclusions. In addition, we showed the effects of the employed penalization factors on the designs. Now, we extend our consideration to dynamic loads. As stated before, it is important to consider the effect of dynamic loads in designing EHDs to continuously harvest electric energy. Therefore, in this example, we consider an optimization problem with the same FE model as the first example with a dynamic point load, as shown in Fig. 11, with the penalization combination of [1 3 1].

Before an optimization considering the dynamic point load, the frequency response curves of the electric energy from 0 Hz to 8000 Hz, as shown in Fig. 12a, and the conversion factor in (b) are calculated and plotted. Two resonance peaks are observed because of the resonances of the system level. To test the effects of excitation frequencies on the optimized layouts, the three excitation frequencies before and after the first resonance frequency

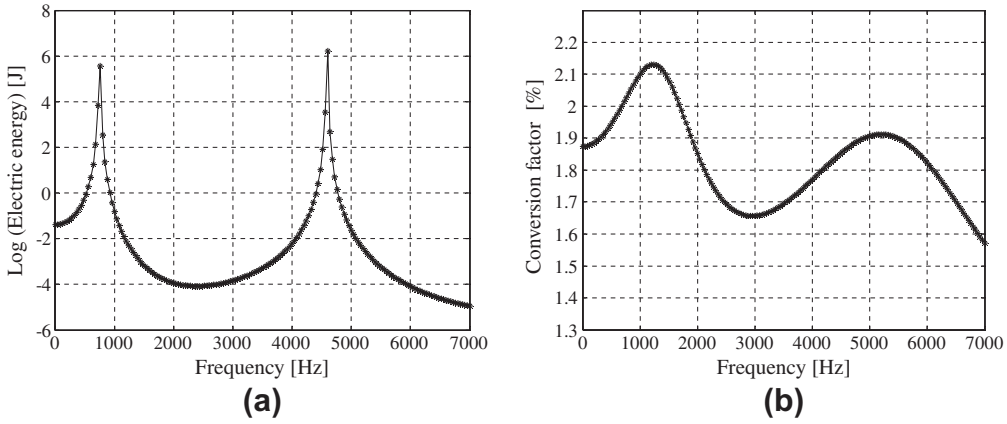

Fig. 12. Initial FRFs of the electric energy and conversion factor considering a dynamic point load (penalization values: [1 3 1]).

are tested. First, by maximizing the dynamic conversion factors for the three excitation frequencies, the layouts are obtained in Fig. 13. As expected, topologically different and disconnected layouts can be obtained. As experienced in the TO of dynamic structures, a layout similar to that with a static load can be obtained for an excitation frequency of 500 Hz. It provides a designguide line that if the frequency ranges of external loads are less than the first eigenfrequencies of EHDs, it is possible to use the static analysis and optimization methods [4]. However, with excitation frequencies of 1000 and 2000 Hz, disconnected domains, i.e., no material near the excitation point, are obtained even with [1 3 1] because the designs have higher dynamic energy conversion factors with higher strain energy values and higher electric energy values. It is also observed that each design is optimized for its excitation frequency.

$$\begin{aligned} &\text{Max} \quad \eta \text{ (Dynamic energy conversion factor)} \\ &\text{s.t} \quad \sum_{e=1}^{NED} \gamma_e v_e \leqslant V^* \ (V^* : \ 60\%) \end{aligned} \tag{21}$$

As observed in the previous numerical examples, the following optimization formulation that maximizes the dynamic electric energy with the static strain energy constraint is also tested. We want to emphasize that the static strain energy constraint is additionally considered rather than the dynamic strain energy constraint.

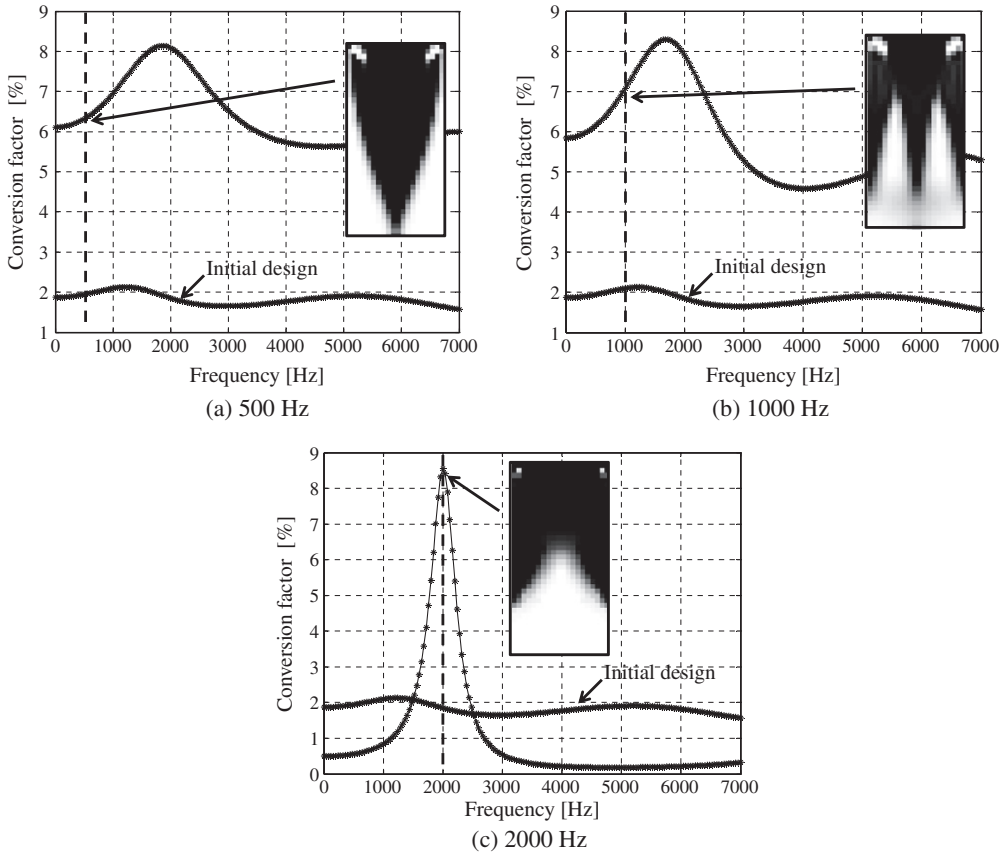

Fig. 13. Optimization results maximizing the energy conversion factor considering a dynamic load (penalization values: [1 3 1]).

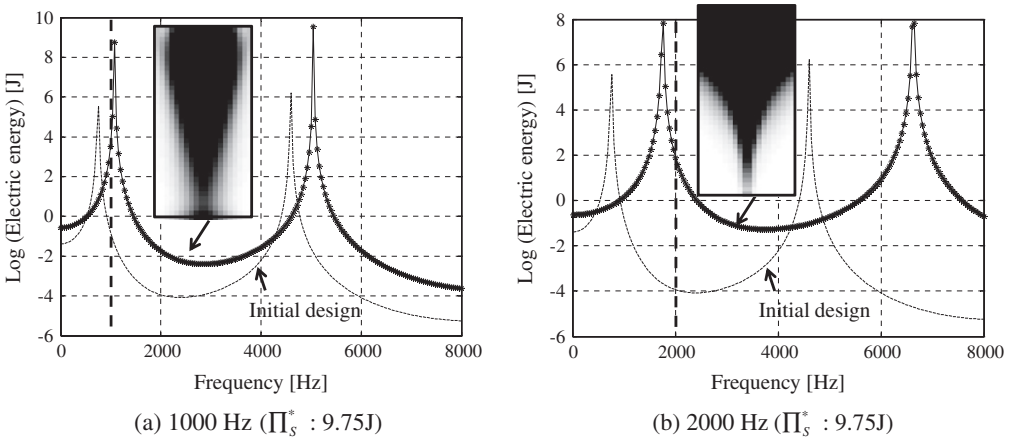

Fig. 14. Optimization results with a static strain energy constraint.

Various upper bounds of the static strain energy are experimentally tested and the layouts with 9.75 J as the upper bound of the static strain energy are presented. Because of the static strain energy constraint, as shown in Fig. 14, the connected domains maximizing the dynamic electric energy can be obtained for excitation frequencies of 1000 and 2000 Hz. Although this has not been presented here, it was possible to consider higher excitation frequencies and it was possible to consider a static strain energy constraint rather than a dynamic strain energy constraint.

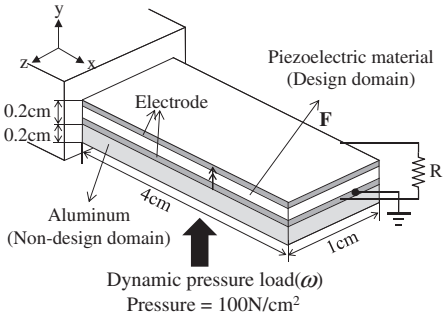

Fig. 15. Problem definition for topology optimization with a dynamic pressure load.

$$\begin{aligned} \text{Max} \quad & \Phi = \prod_{E} (\text{Dynamic electric energy} \\ \text{s.t.} \quad & \sum_{e=1}^{NED} \gamma_e v_e \leqslant V^* \\ & \prod_{S} \leqslant \prod_{S}^{*} \left(\prod_{S}^{*} : \text{The upper bound of the static strain energy} \right) \end{aligned} \tag{22}$$

4.4. Example 4: Maximizing power subject to dynamic strain energy for a dynamic pressure load

For the last numerical example, we consider the structure in Fig. 15 having a similar domain to that in Example 3 using the optimization formulation (23). To consider the dynamic pressure load for an excitation frequency of 500 Hz, the aluminum plate is reconsidered. It is seen in Fig. 16 that the power graph of this structure with a uniform initial density (γ_{init} = 0.6) is almost similar to that in

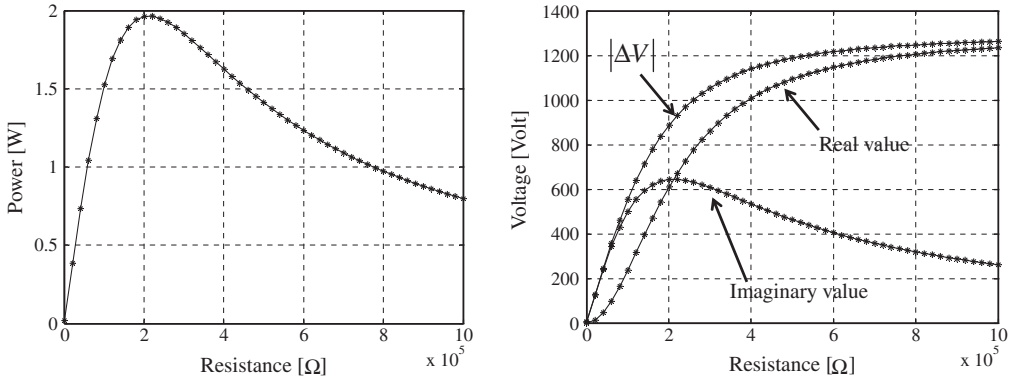

Fig. 16. Curves of the power and voltage considering the dynamic pressure load of 500 Hz (penalization values: [1 3 1]).

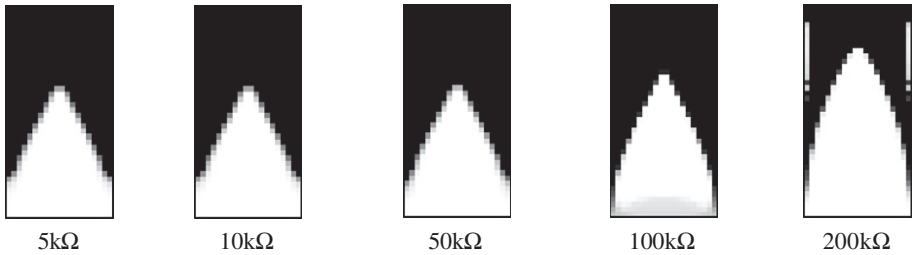

(a)

Frequency = 500 Hz					
Resistance (Ω)	5kΩ	10kΩ	50kΩ	100kΩ	200kΩ
Dynamic strain energy (J)	0.0610	0.0610	0.0601	0.0601	0.0696
Dynamic electric energy (J)	0.0018	0.0018	0.0021	0.0027	0.0036
Power (W)	0.5980	1.1908	5.2383	7.9055	10.999

(b)

Fig. 17. Optimization results with different resistance values at 500 Hz ($\prod_S^*$ = 0.06J, penalization values: [1 3 1]).

Example 5. From several numerical tests, the upper bound of the static strain energy is set to 0.06 J. The optimal layouts are presented in Fig. 17 and they differ because of the loading condition and aluminum plate. Therefore, this example verifies the importance of the consideration of the dynamic power and the static constraint in optimization.

$$\begin{aligned} &\text{Max}\Phi = \text{Power} \\ &\text{s.t.} \quad \sum_{e=1}^{NED} \gamma_e \mathrm{v}_e \leqslant V^* \ (V^* : \ 60\%) \\ &\prod_S \leqslant \prod_S^* \left(\prod_S^* : \ \text{The upper bound of the static strain energy} \right) \end{aligned} \tag{23}$$

5. Conclusions

A systematic design approach to improve the efficiencies of energy harvesting devices (EHDs) through topology optimization (TO) for static and dynamic loads is studied and presented. This approach is based on three-dimensional FE models for dynamic piezoelectric EHDs. For this purpose, an in-house FE code using standard 8-node elements having the structural displacements and potential as degrees of freedom is developed. The developed FE code can also consider external circuits to simulate externally isolated systems (passive electrical networks) such as a motor or heater. By solving several optimization and analysis examples, this research reconfirms that the piezoelectric based EHD cannot generate a DC voltage. In order to obtain continuous electric energy from EHDs, continuous excitation forces should be applied. By investigating the optimization results, it is observed that the vibration-powered EHDs provide the maximum voltage and power outputs when operated at resonances but it is not always guaranteed due to ill-controllable random force frequency. In other words, the frequency bands of excitation force should be considered when the layouts of EHD and an electric circuit are designed. For EHDs for excitation forces over a broad bandwidth, the optimized structures at the excitation frequencies should be integrated. Depending on the objective functions such as static and dynamic electric energies and energy conversion factors, different optimized layouts can be obtained. The study of the configuration of the piezoelectric and non-piezoelectric materials reconfirms that the domain and boundary configurations play an important role in the distributions of the extension and compression stresses within a piezoelectric material. Thus, it is important to choose a proper configuration of the piezoelectric material and substrate (non-piezoelectric material) to prevent a short-circuit within the electrodes and piezoelectric material before TO.

The versatility of the developed method is also demonstrated by several illustrative analyses and optimization examples. The obtained results reveal that depending on the penalization values of SIMP used to interpolate the material properties, the behaviors of the electric and elastic energies differ. Therefore, we suffer from the local optima in TO and disconnected designs. To resolve these issues, different optimization formulations with static or dynamic compliance are studied and tested. For continuous EHDs, the effect of dynamic loads on optimal layouts is also studied. As experienced in the structural optimization, the inclusion of dynamic load leads to different layouts. Depending on the kind of load and a configuration of piezoelectric material and substrate with a circuit, different layouts should be used. For dynamic load whose excitation frequency is below the first peak of the object function such as power, electric energy, and conversion factor, it is likely that static results can be used. But dynamic loads with higher excitation frequencies, the present approach should be considered. Furthermore, with electric resistor or structural damping, the same layouts can be obtained but the magnitudes of objective functions can be different. Obviously, the developed FE code and optimization formulations can be applied to any other EHD for a different mechanical loading condition, a different configuration of piezoelectric and non-piezoelectric materials, and other piezoelectric materials such as PVDF.

In future studies, we believe that it will be of interest to consider multiphysics systems involving a fluid, electric energy, and a structure together. For example, we can design a flow channel made of a piezoelectric material to maximize the efficiency of EHDs, including the design of the number of layers through TO. Because the sort-circuit within the PZT structure affects performance, the type of layered PZT EHD should be optimized by topology optimization (see Appendix B). In addition, it is possible to consider a wide range of frequency ranges of interest for powering autonomous sensors and actuators from background random vibrations. For this future research subject, it may be possible to adopt the model order reduction scheme for efficient response calculations. It is also possible to extend this study to consider the manufacturability because of the material characteristics of piezoelectric materials and to consider the pulsation load exciting broadband frequencies.

Acknowledgement

This work was supported by the research fund of Hanyang University (HY-2011-N).

Appendix A. Relationship between structural resonances and electrical resonances

From several numerical tests, it is found that there are strong relationships between the resonances of the structural system and those of the electric system. Not presented here in detail, it can be observed that some of the structural resonance peaks

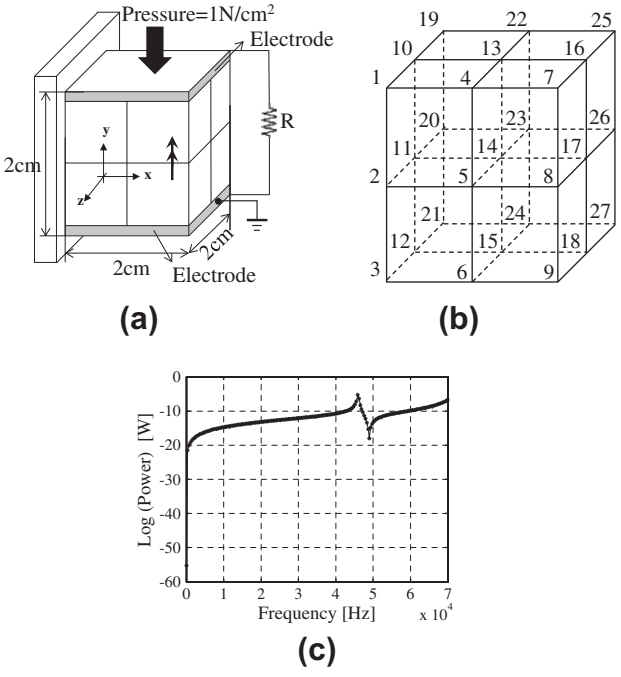

Fig. 18. A PZT plate with a resistor. (a) An FE model (1st : 19774 Hz, 2nd : 20951 Hz, 3rd :26273 Hz, 4th: 47956 Hz, 5th: 54860 Hz, 6th:58812 Hz), (b) node number, and (c) power curve (Power $= \frac{|\Delta V^2|}{2R}$, R = 1 kΩ).

exactly match the eigenfrequencies. Furthermore, at electrodes, because of a short-circuit at the electrode domains only some resonance peaks of the voltage are observed. Therefore, although we maximize the electric energy at a certain frequency or in certain frequency ranges, the output voltage may not be maximized because of the effect of electrodes, indicating that there is a need to optimize the shape of the electrodes simultaneously. However, this is beyond the scope of this study. The observations can be extended to the model having the same condition but with a resistor. As noted in the previous section, the inclusion of the resistor imposes a nonlinear damping effect on the overall systems. One of the important aspects is that it becomes possible to directly measure the harvested power from the model shown in Fig. 18a. Fig. 19 shows the frequency response of energies, voltages, and displacements.

A comparison of the conversion factors of the two structures (Figs. 18 and 19), as shown in Fig. 20a, reconfirms that the curves of the conversion factors are highly nonlinear and will suffer from the local optima in TO. Fig. 20b shows voltage curves with various resistor values to show the nonlinear damping effect of the resistor.

Appendix B. Layered PZT-based energy harvesting devices

To the best of our knowledge, several layered structures, referred to as unimorph (having a single piezoelectric layer for actuation), bimorph (having two piezoelectric layers for actuation), and multimorph (having more than two piezoelectric layers for actuation) with and without substrates (non-piezoelectric) exist, as shown in Fig. 21. The first structure consists of a single PZT structure whereas the second and third structures consist of both piezoelectric materials and the substrate (non-piezoelectric material). In the first unimorph structure without an elastic body, all mechanical and electric loads are stored in the piezoelectric body; in contract, mechanical energies are also distributed in the substrates in the cases of the bimorph and multimorph structures. From the viewpoint of energy, it appears that the first structure not sharing electric energy with the substrates is efficient relative to the other two structures. However, because of the short-circuit within the PZT structure, the first structure is found to be less efficient than the other two structures. In other words, in the unimorph case, the positive and negative electric fields generated by the bending stresses along a normal face are short-circuited that results in no

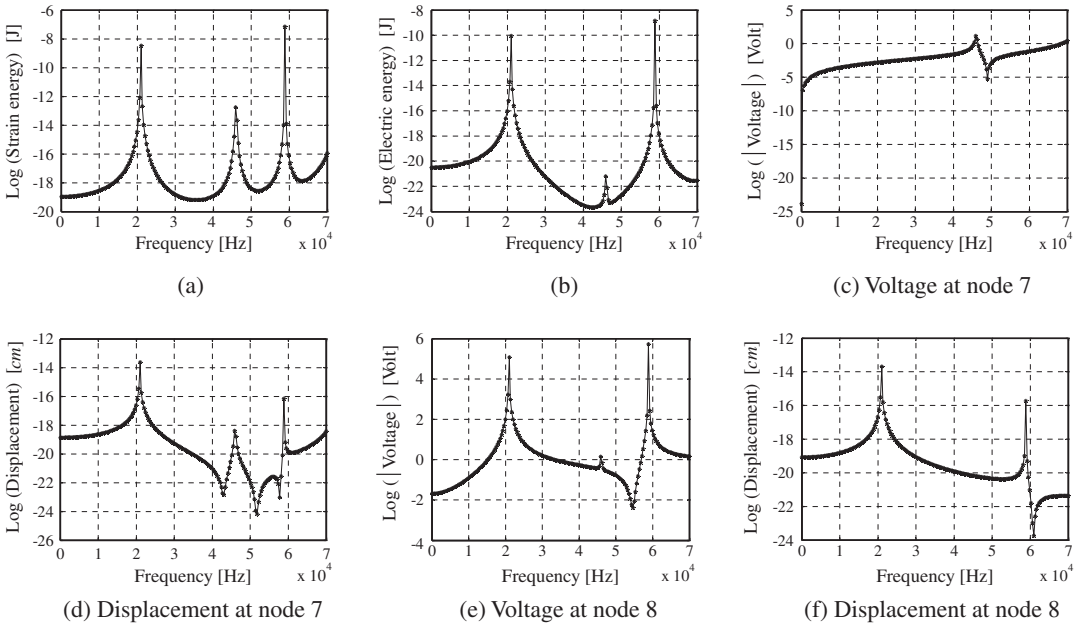

Fig. 19. Frequency responses of energies, voltages, and displacements.

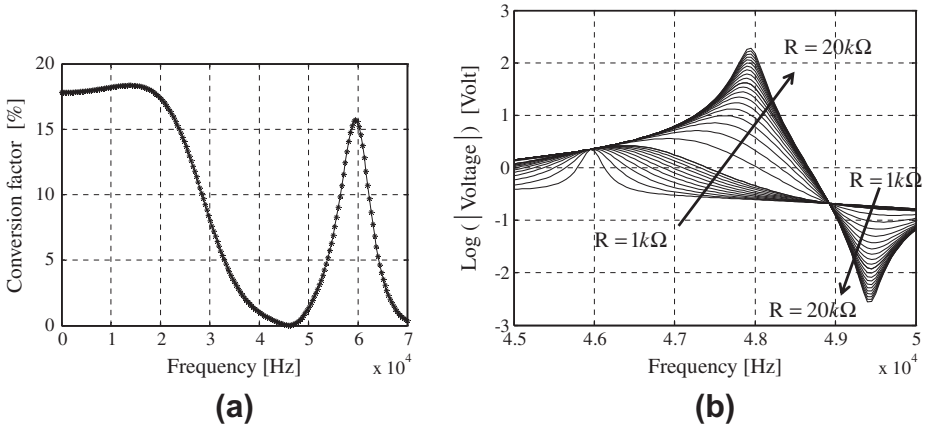

Fig. 20. (a) Curves of conversion factor of Fig. 19 and curves of voltages considering different resistance values.

electric energy. Therefore, it is common to use these layered structures having compression or tension only stress to piezoelectric materials. From the viewpoint of optimization, we can design this optimal configuration with the piezoelectric material and the substrate. However, this is beyond the scope of this study.

Depending on their configuration and boundary condition, EHDs can have very complex characteristics. To illustrate this phenomenon, we calculate the energy conversion factors for the case with different quasi-static mechanical loads; the results are shown in Fig. 22. The first structure consists of the upper PZT structure and the bottom aluminum panel with the load at the end tip whereas the pressure load is applied to the second structure. As shown in the figures, the elastic and electric energies decrease with an increase in the thickness values of the aluminum substrates because the structures obviously become stiffer. However, as shown in Fig. 22, the behaviors of the conversion factor and the voltage at

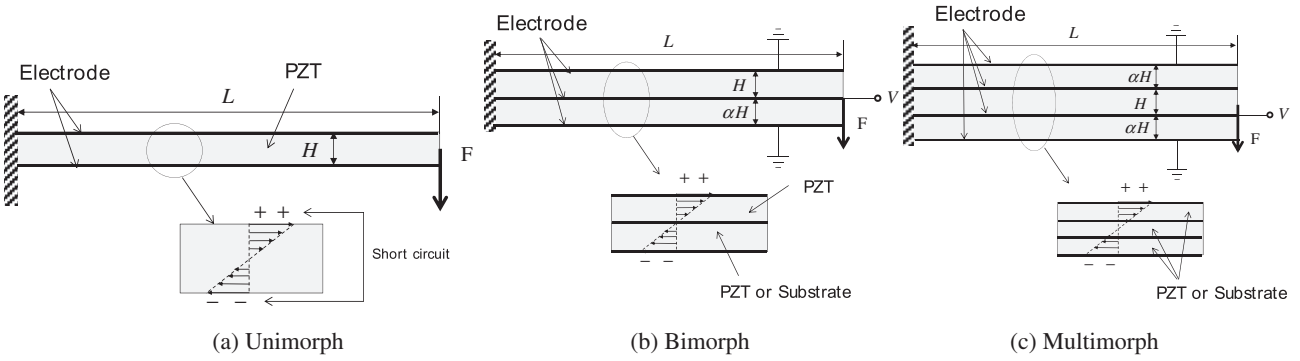

Fig. 21. Unimorph, bimorph, and multimorph PZT energy harvesting devices (α: an arbitrary number).

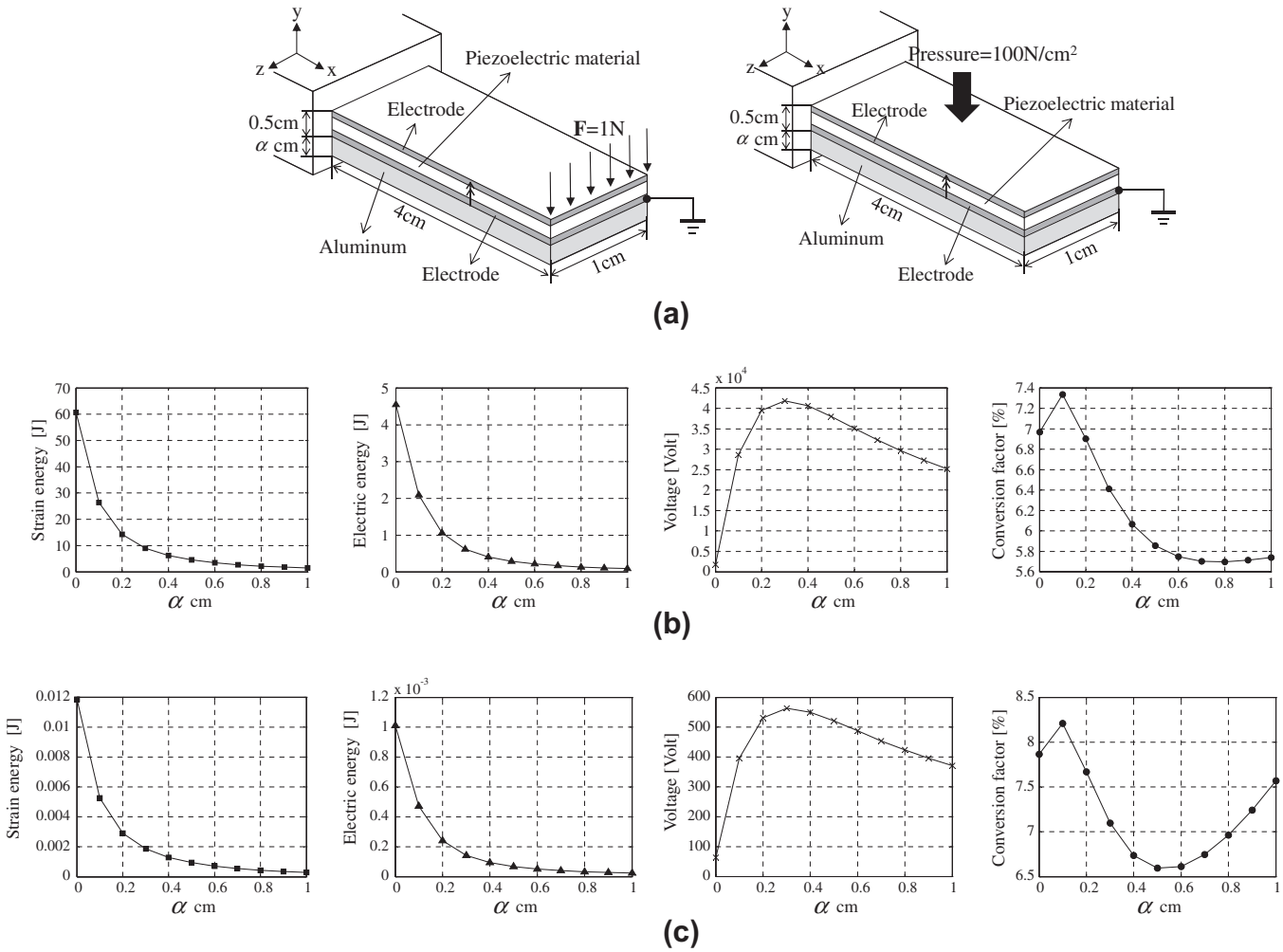

Fig. 22. Bimorph test model with different thickness values for a point load (aluminum substrate: ρ = 2700 kg/m^3, E = 73.0 GPa, ν = 0.33)). (a) Problem definition, (b) curves of the elastic energy, electric energy, voltage of top electrode, and conversion factor of Left of (a), and (c) curves of the elastic energy, electric energy, voltage of top electrode, and conversion factor of Right of (a).

the top plate of the two structures differ considerably from each other. In particular, the energy conversion factors exhibit highly nonlinear curves with respect to the thickness values of the aluminum plate. These numerical tests suggest that we will suffer from many local optima in TO.

Appendix C. Sensitivity analysis

C.1. Static responses and sensitivity analysis

To use a gradient-based optimizer, it is essential to derive the sensitivity analysis for a given objective function. To define objective functions that maximize the efficiency for piezoelectric EHDs and to derive the complex sensitivities of functions, some energy functions using static responses are first defined. First, the quasi-static responses are calculated by solving the following equation.

$$\text{Static analysis}: \quad \begin{bmatrix} \mathbf{K_{uu}} & \mathbf{K_{u\varphi}} \\ \mathbf{K_{\varphi u}} & -\mathbf{K_{\varphi\varphi}} \end{bmatrix} \begin{bmatrix} \mathbf{u} \\ \boldsymbol{\varphi} \end{bmatrix} = \begin{bmatrix} \mathbf{F} \\ \mathbf{Q} \end{bmatrix} \tag{24}$$

Then, a general function form can be defined as follows:

$$\text{General form of objective function}: \quad \Phi = [\mathbf{u}\boldsymbol{\varphi}]\mathbf{A}\begin{bmatrix} \mathbf{u} \\ \boldsymbol{\varphi} \end{bmatrix} \tag{25}$$

where $\mathbf{A}$ is an arbitrary matrix defining an energy form. By differentiating this energy form Φ with respect to a design variable (γ_e), the following sensitivity analysis can be obtained:

$$\frac{\partial \Phi}{\partial \gamma_e} = 2[\mathbf{u}\boldsymbol{\varphi}]\mathbf{A}\begin{bmatrix} \frac{\partial \mathbf{u}}{\partial \gamma_e} \\ \frac{\partial \boldsymbol{\varphi}}{\partial \gamma_e} \end{bmatrix} + [\mathbf{u}\ \boldsymbol{\varphi}]\frac{\partial \mathbf{A}}{\partial \gamma_e}\begin{bmatrix} \mathbf{u} \\ \boldsymbol{\varphi} \end{bmatrix} \tag{26}$$

To efficiently calculate $\left[\frac{\partial \mathbf{u}}{\partial \gamma_e}\partial\boldsymbol{\varphi}\partial\gamma_e\right]$, the adjoint sensitivity analysis is employed. By differentiating the governing equation, the following equation is obtained.

$$\begin{bmatrix} \frac{\partial \mathbf{u}}{\partial \gamma_e} \\ \frac{\partial \boldsymbol{\varphi}}{\partial \gamma_e} \end{bmatrix} = -\begin{bmatrix} \mathbf{K_{uu}} & \mathbf{K_{u\varphi}} \\ \mathbf{K_{\varphi u}} & -\mathbf{K_{\varphi\varphi}} \end{bmatrix}^{-1} \begin{bmatrix} \frac{\partial \mathbf{K_{uu}}}{\partial \gamma_e} & \frac{\partial \mathbf{K_{u\varphi}}}{\partial \gamma_e} \\ \frac{\partial \mathbf{K_{\varphi u}}}{\partial \gamma_e} & -\frac{\partial \mathbf{K_{\varphi\varphi}}}{\partial \gamma_e} \end{bmatrix} \begin{bmatrix} \mathbf{u} \\ \boldsymbol{\varphi} \end{bmatrix} \tag{27}$$

And the variables $\left[\frac{\partial \mathbf{u}}{\partial \gamma_e}\partial\boldsymbol{\varphi}\partial\gamma_e\right]$ of (26) are replaced by with (27). Then, we introduce the following adjoint equation.

$$\begin{bmatrix} \mathbf{K_{uu}} & \mathbf{K_{u\varphi}} \\ \mathbf{K_{\varphi u}} & -\mathbf{K_{\varphi\varphi}} \end{bmatrix}^{\mathrm{T}} \begin{bmatrix} \boldsymbol{\lambda_u} \\ \boldsymbol{\lambda_\varphi} \end{bmatrix} = \mathbf{A}^{\mathrm{T}} \begin{bmatrix} \mathbf{u} \\ \boldsymbol{\varphi} \end{bmatrix} \tag{28}$$

where $[\boldsymbol{\lambda_u}\boldsymbol{\lambda_\varphi}]$ are adjoint variables. By substituting these variables in Eq. (26), the following sensitivity analysis is obtained:

$$\frac{\partial \Phi}{\partial \gamma_e} = -2[\boldsymbol{\lambda_u}\boldsymbol{\lambda_\varphi}]\begin{bmatrix} \frac{\partial \mathbf{K_{uu}}}{\partial \gamma_e} & \frac{\partial \mathbf{K_{u\varphi}}}{\partial \gamma_e} \\ \frac{\partial \mathbf{K_{\varphi u}}}{\partial \gamma_e} & -\frac{\partial \mathbf{K_{\varphi\varphi}}}{\partial \gamma_e} \end{bmatrix}\begin{bmatrix} \mathbf{u} \\ \boldsymbol{\varphi} \end{bmatrix} + [\mathbf{u}\boldsymbol{\varphi}\frac{\partial \mathbf{A}}{\partial \gamma_e}\begin{bmatrix} \mathbf{u} \\ \boldsymbol{\varphi} \end{bmatrix} \tag{29}$$

Using the above derivation, the sensitivity analyses of the elastic energy, electric energy, and conversion factor can be derived as follows:

$$\begin{aligned} \text{Elastic energy (strain energy)}: \quad \Pi_S &= \frac{1}{2}\mathbf{u}^{\mathrm{T}}\mathbf{K_{uu}}\mathbf{u} \\ &= \frac{1}{2}\begin{bmatrix} \mathbf{u} \\ \boldsymbol{\varphi} \end{bmatrix}^{\mathrm{T}}\begin{bmatrix} \mathbf{K_{uu}} & 0 \\ 0 & 0 \end{bmatrix}\begin{bmatrix} \mathbf{u} \\ \boldsymbol{\varphi} \end{bmatrix} \end{aligned} \tag{30}$$

$$\begin{aligned} \frac{\partial \Pi_S}{\partial \gamma_e} = &-\begin{bmatrix} \mathbf{u} \\ \boldsymbol{\varphi} \end{bmatrix}^{\mathrm{T}}\begin{bmatrix} \mathbf{K_{uu}} & 0 \\ 0 & 0 \end{bmatrix}\begin{bmatrix} \mathbf{K_{uu}} & \mathbf{K_{u\varphi}} \\ \mathbf{K_{\varphi u}} & -\mathbf{K_{\varphi\varphi}} \end{bmatrix}^{-1}\begin{bmatrix} \frac{\partial \mathbf{K_{uu}}}{\partial \gamma_e} & \frac{\partial \mathbf{K_{u\varphi}}}{\partial \gamma_e} \\ \frac{\partial \mathbf{K_{\varphi u}}}{\partial \gamma_e} & -\frac{\partial \mathbf{K_{\varphi\varphi}}}{\partial \gamma_e} \end{bmatrix}\begin{bmatrix} \mathbf{u} \\ \boldsymbol{\varphi} \end{bmatrix} \\ &+\frac{1}{2}\begin{bmatrix} \mathbf{u} \\ \boldsymbol{\varphi} \end{bmatrix}^{\mathrm{T}}\begin{bmatrix} \frac{\partial \mathbf{K_{uu}}}{\partial \gamma_e} & 0 \\ 0 & 0 \end{bmatrix}\begin{bmatrix} \mathbf{u} \\ \boldsymbol{\varphi} \end{bmatrix} \end{aligned} \tag{31}$$

$$\text{Electric energy}: \quad \Pi_E = \frac{1}{2}\boldsymbol{\varphi}^{\mathrm{T}}\mathbf{K_{\varphi\varphi}}\boldsymbol{\varphi} = \frac{1}{2}\begin{bmatrix} \mathbf{u} \\ \boldsymbol{\varphi} \end{bmatrix}^{\mathrm{T}}\begin{bmatrix} 0 & 0 \\ 0 & \mathbf{K_{\varphi\varphi}} \end{bmatrix}\begin{bmatrix} \mathbf{u} \\ \boldsymbol{\varphi} \end{bmatrix} \tag{32}$$

$$\begin{aligned} \frac{\partial \Pi_S}{\partial \gamma_e} = &-\begin{bmatrix} \mathbf{u} \\ \boldsymbol{\varphi} \end{bmatrix}^{\mathrm{T}}\begin{bmatrix} 0 & 0 \\ 0 & \mathbf{K_{uu}} \end{bmatrix}\begin{bmatrix} \mathbf{K_{uu}} & \mathbf{K_{u\varphi}} \\ \mathbf{K_{\varphi u}} & -\mathbf{K_{\varphi\varphi}} \end{bmatrix}^{-1}\begin{bmatrix} \frac{\partial \mathbf{K_{uu}}}{\partial \gamma_e} & \frac{\partial \mathbf{K_{u\varphi}}}{\partial \gamma_e} \\ \frac{\partial \mathbf{K_{\varphi u}}}{\partial \gamma_e} & -\frac{\partial \mathbf{K_{\varphi\varphi}}}{\partial \gamma_e} \end{bmatrix}\begin{bmatrix} \mathbf{u} \\ \boldsymbol{\varphi} \end{bmatrix} \\ &+\frac{1}{2}\begin{bmatrix} \mathbf{u} \\ \boldsymbol{\varphi} \end{bmatrix}^{\mathrm{T}}\begin{bmatrix} 0 & 0 \\ 0 & \frac{\partial \mathbf{K_{uu}}}{\partial \gamma_e} \end{bmatrix}\begin{bmatrix} \mathbf{u} \\ \boldsymbol{\varphi} \end{bmatrix} \end{aligned} \tag{33}$$

$$\begin{aligned} \text{Energy conversion factor}: \eta &= \frac{\frac{1}{2}\boldsymbol{\phi}^{\mathrm{T}}\mathbf{K_{\varphi\varphi}}\boldsymbol{\varphi}}{\frac{1}{2}\mathbf{u}^{\mathrm{T}}\mathbf{K_{uu}}\mathbf{u} + \frac{1}{2}\boldsymbol{\varphi}^{\mathrm{T}}\mathbf{K_{\varphi\varphi}}\boldsymbol{\varphi}} \\ &= \frac{\Pi_E}{\Pi_S + \Pi_E} \end{aligned} \tag{34}$$

$$\frac{\partial \eta}{\partial \gamma_e} = \frac{\frac{\partial \Pi_E}{\partial \gamma_e}(\Pi_S + \Pi_E) - \Pi_E\left(\frac{\partial \Pi_S}{\partial \gamma_e} + \frac{\partial \Pi_E}{\partial \gamma_e}\right)}{(\Pi_S + \Pi_E)^2} \tag{35}$$

Using the objective values and the sensitivity analyses, TO can be performed.

C.2. Dynamic responses and sensitivity analysis

Most existing studies on TO, except [17], are based on the above static responses and sensitivity analysis. However, in reality, we should consider the dynamic responses for EHDs. From the viewpoint of optimization, it is not clear how the *dynamic* elastic energy, dynamic electric energy, and dynamic conversion factor should be defined. This paper defines the dynamic elastic and electric energies from discussions of previous studies regarding the TO of dynamic compliance. The dynamic responses are calculated from the following equation.

$$\left\{-\omega^2\begin{bmatrix} \mathbf{M} & \mathbf{0} \\ \mathbf{0} & \mathbf{0} \end{bmatrix} + i\omega\mathbf{C} + \begin{bmatrix} \mathbf{K_{uu}} & \mathbf{K_{u\varphi}} \\ \mathbf{K_{\varphi u}} & -\mathbf{K_{\varphi\varphi}} \end{bmatrix} - \frac{i}{\omega}\sum_{j=1}^{NR}\frac{1}{\mathrm{R}_j}\right\}\begin{bmatrix} \mathbf{u} \\ \boldsymbol{\varphi} \end{bmatrix} = \mathbf{S}\begin{bmatrix} \mathbf{u} \\ \boldsymbol{\varphi} \end{bmatrix}\begin{bmatrix} \mathbf{F} \\ \mathbf{Q} \end{bmatrix} \tag{36}$$

Note that because the solutions of the above equation are complex, the complex sensitivity analysis should be derived. To make it clear, the dynamic stiffness matrix, $\mathbf{S}$, is introduced. For a general formulation, the following objective is considered.

$$\text{General form of objective function}: \quad \Phi = [\bar{\mathbf{u}}\bar{\boldsymbol{\varphi}}]\mathbf{A}\begin{bmatrix} \mathbf{u} \\ \boldsymbol{\varphi} \end{bmatrix} \tag{37}$$

where $\mathbf{A}$ is a general matrix and the variables with upper bars indicate the complex conjugates of the corresponding variables. By differentiating the governing equation and the objective, the following equations are obtained.

$$\frac{\partial \Phi}{\partial \gamma_e} = \left[\frac{\partial \bar{\mathbf{u}}}{\partial \gamma_e}\ \frac{\partial \bar{\boldsymbol{\varphi}}}{\partial \gamma_e}\right]\mathbf{A}\begin{bmatrix} \mathbf{u} \\ \boldsymbol{\varphi} \end{bmatrix} + [\bar{\mathbf{u}}\bar{\boldsymbol{\varphi}}]\frac{\partial \mathbf{A}}{\partial \gamma_e}\begin{bmatrix} \mathbf{u} \\ \boldsymbol{\varphi} \end{bmatrix} + [\bar{\mathbf{u}}\bar{\boldsymbol{\varphi}}]\frac{\partial \mathbf{A}}{\partial \gamma_e}\begin{bmatrix} \frac{\partial \mathbf{u}}{\partial \gamma_e} \\ \frac{\partial \boldsymbol{\varphi}}{\partial \gamma_e} \end{bmatrix} \tag{38}$$

$$\begin{bmatrix} \frac{\partial \mathbf{u}}{\partial \gamma_e} \\ \frac{\partial \boldsymbol{\varphi}}{\partial \gamma_e} \end{bmatrix} = -\mathbf{S}^{-1}\frac{\partial \mathbf{S}}{\partial \gamma_e}\begin{bmatrix} \mathbf{u} \\ \boldsymbol{\varphi} \end{bmatrix}, \begin{bmatrix} \frac{\partial \bar{\mathbf{u}}}{\partial \gamma_e} \\ \frac{\partial \bar{\boldsymbol{\varphi}}}{\partial \gamma_e} \end{bmatrix} = -\bar{\mathbf{S}}^{-1}\frac{\partial \bar{\mathbf{S}}}{\partial \gamma_e}\begin{bmatrix} \bar{\mathbf{u}} \\ \bar{\boldsymbol{\varphi}} \end{bmatrix} \tag{39}$$

For the efficient sensitivity analysis, the differentiations of structural and electric displacements of (38) are replaced by the Eq. (39). Through some algebraic manipulation, the complex adjoint variables are defined as follows:

$$\left\{-\omega^2\begin{bmatrix} \mathbf{M} & \mathbf{0} \\ \mathbf{0} & \mathbf{0} \end{bmatrix} + i\omega\mathbf{C} + \begin{bmatrix} \mathbf{K_{uu}} & \mathbf{K_{u\varphi}} \\ \mathbf{K_{\varphi u}} & -\mathbf{K_{\varphi\varphi}} \end{bmatrix} - \frac{i}{\omega}\sum_{j=1}^{NR}\frac{1}{\mathrm{R}_j}\right\}^{\mathrm{T}}\begin{bmatrix} \boldsymbol{\lambda_u} \\ \boldsymbol{\lambda_\varphi} \end{bmatrix} = -\mathbf{A}^{\mathrm{T}}\begin{bmatrix} \bar{\mathbf{u}} \\ \bar{\boldsymbol{\varphi}} \end{bmatrix} \tag{40}$$

Through some algebraic manipulation, the following sensitivity analysis can be derived.

$$\frac{\partial \Phi}{\partial \gamma_e} = [\bar{\mathbf{u}}\bar{\boldsymbol{\varphi}}]\frac{\partial \mathbf{A}}{\partial \gamma_e}\begin{bmatrix}\mathbf{u}\\ \boldsymbol{\varphi}\end{bmatrix} + 2Real\left([\boldsymbol{\lambda}_{\mathbf{u}}\boldsymbol{\lambda}_{\boldsymbol{\varphi}}]\frac{\partial \mathbf{S}_e}{\partial \gamma_e}\begin{bmatrix}\mathbf{u}\\ \boldsymbol{\varphi}\end{bmatrix}\right) \tag{41}$$

In this paper, we define the dynamic elastic energy, dynamic electric energy, and dynamic energy conversion factor as follows:

$$\text{Elastic energy (strain energy)}: \ \Pi_S = \frac{1}{2}\bar{\mathbf{u}}^{\mathrm{T}}\mathbf{K}_{\mathbf{uu}}\mathbf{u} = \frac{1}{2}\begin{bmatrix}\bar{\mathbf{u}}\\ \bar{\boldsymbol{\varphi}}\end{bmatrix}^{\mathrm{T}}\begin{bmatrix}\mathbf{K}_{\mathbf{uu}} & 0\\ 0 & 0\end{bmatrix}\begin{bmatrix}\mathbf{u}\\ \boldsymbol{\varphi}\end{bmatrix} \tag{42}$$

$$\text{Electric energy}: \ \Pi_E = \frac{1}{2}\bar{\boldsymbol{\varphi}}^{\mathrm{T}}\mathbf{K}_{\boldsymbol{\varphi}\boldsymbol{\varphi}}\boldsymbol{\varphi} = \frac{1}{2}\begin{bmatrix}\bar{\mathbf{u}}\\ \bar{\boldsymbol{\varphi}}\end{bmatrix}^{\mathrm{T}}\begin{bmatrix}0 & 0\\ 0 & \mathbf{K}_{\boldsymbol{\varphi}\boldsymbol{\varphi}}\end{bmatrix}\begin{bmatrix}\mathbf{u}\\ \boldsymbol{\varphi}\end{bmatrix} \tag{43}$$

$$\text{Energy conversion factor}: \ \eta = \frac{\frac{1}{2}\bar{\boldsymbol{\phi}}^{\mathrm{T}}\mathbf{K}_{\boldsymbol{\varphi}\boldsymbol{\varphi}}\boldsymbol{\varphi}}{\frac{1}{2}\bar{\mathbf{u}}^{\mathrm{T}}\mathbf{K}_{\mathbf{uu}}\mathbf{u} + \frac{1}{2}\bar{\boldsymbol{\varphi}}^{\mathrm{T}}\mathbf{K}_{\boldsymbol{\varphi}\boldsymbol{\varphi}}\boldsymbol{\varphi}} = \frac{\Pi_E}{\Pi_S + \Pi_E} \tag{44}$$

The sensitivity analyses of the above energies and the factor can be easily obtained by applying the derived adjoint sensitivity analysis method.

The above analysis procedures and sensitivity analyses are implemented in the framework of MATLAB and are verified by the finite difference method. In addition, the optimization procedure shown in Fig. 4 is implemented with the method of moving asymptotes (MMA) [34] for an optimization algorithm.

References

[1] Sodano HA, Inman DJ, Gyuhae Park. A review of power harvesting from vibration using piezoelectric materials. Shock Vib Dig 2004;36(3):197–205.
[2] Standard committee of the IEEE ultrasonics, ferroelectrics, and frequency control society. IEEE standard on piezoelectricity. The Institute of Electrical and Electronics Engineers, Inc., New York; 1988.
[3] Carrera E, Brischetto S, Nali P. Plates and shells for smart structures: classical and advanced theories for modeling and analysis. John Wiley & Sons; 2011.
[4] Zheng B, Chang CJ, Gea HC. Topology optimization of energy harvesting devices using piezoelectric materials. Struct Multidiscip Optim 2009;38(1):17–23.
[5] Rupp CJ, Evgrafov A, Maute K, Dunn ML. Design of piezoelectric energy harvesting systems: a topology optimization approach based on multilayer plates and shells. J Intell Mater Syst Struct 2009;20(16):1923–39.
[6] Silva ECN, Kikuchi N. Design of piezoelectric transducers using topology optimization. Smart Mater Struct 1999;8(3):350–64.
[7] Silva ECN, Fonseca O, Espinosa MD, Crumm AT, Brady GA, Halloran JW, et al. Design of piezoelectric materials and piezoelectric transducers using topology optimization – part I. Arch Comput Methods Eng 1999;6(2):117–82.
[8] Silva ECN, Nishiwaki S, Kikuchi N. Design of piezocomposite materials and piezoelectric transducers using topology optimization – part II. Arch Comput Methods Eng 1999;6(3):191–222.
[9] Donoso A, Sigmund O. Optimization of piezoelectric bimorph actuators with active damping for static and dynamic loads. Struct Multidiscip Optim 2009;38(2):171–83.
[10] Donoso A, Bellido JC, Chacon JM. Numerical and analytical method for the design of piezoelectric modal sensors/actuators for shell-type structures. Int J Numer Methods Eng 2010;81:1700–12.
[11] Choi JS, Yoo JH. Simultaneous structural topology optimization of electromagnetic sources and ferromagnetic materials. Comput Methods Appl Mech Eng 2009;198(27–29):2111–21.
[12] Bendsøe MP, Sigmund O. Topology optimization theory, methods and applications. Berlin: Springer; 2003.
[13] Pedersen NL. Maximization of eigenvalues using topology optimization. Struct Multidiscip Optim 2000;20(1):2–11.
[14] Kang Z, Tong L. Topology optimization-based distribution design of actuation voltage in static shape control of plates. Comput Struct 2008;86(19–20):1885–93.
[15] Canfield S, Frecker M. Topology optimization of compliant mechanical amplifiers for piezoelectric actuators. Struct Multidiscip Optim 2000;20(4):269–79.
[16] Bendsøe MP, Kikuchi N. Generating optimal topologies in structural design using a homogenization method. Comput Methods Appl Mech Eng 1988;71(2):197–224.
[17] Carbonari RC, Silva ECN, Paulino GH. Multi-actuated functionally graded piezoelectric micro-toolsdesign: a multiphysics topology optimization approach. Int J Numer Methods Eng 2009;77(3):301–36.
[18] Carbonari RC, Silva ECN, Nishiwaki S. Optimum placement of piezoelectric material in piezoactuator design. Smart Mater Struct 2007;16(1):207–20.
[19] Silva ECN, Nishiwaki S, Kikuchi N. Topology optimization design of flextensional actuators. IEEE Trans Ultrason Ferroelect Freq Control 2000;47(3):657–71.
[20] Kim JE, Kim DS, Ma PS, Kim YY. Multi-physics interpolation for the topology optimization of piezoelectric systems. Comput Methods Appl Mech Eng 2010;199(49–52):3153–68.
[21] Luo Z, Tong L, Luo J, Wang MY. Design of piezoelectric actuators using a multiphase level set method of piecewise constants. J Comput Phys 2009;228(7):2643–59.
[22] Chen S, Gonella S, Chen W, Liu WK. A level set approach for optimal design of smart energy harvesters. Comput Methods Appl Mech Eng 2010;199(37–40):2532–43.
[23] Bathe KJ. Finite element procedures. New Jersey: Prentice-Hall; 1996.
[24] Cook RD, Malkus DS, Plesha ME, Witt RJ. Concepts and applications of finite element analysis. 4th ed. New Jersey (USA): John Wiley &Sons; 2001.
[25] Lerch R. Finite element analysis of piezoelectric transducers. IEEE Trans Ultrason Symp 1988;2:643–54.
[26] Lerch R. Simulation of piezoelectric devices by two- and three-dimensional finite elements. IEEE Trans Ultrason Ferroelect Freq Control 1990;37(3):233–47.
[27] Allik H, Hughes TJR. Finite element method for piezoelectric vibration. Int J Numer Methods Eng 1970;2(2):151–7.
[28] Shimomura NIT, Harada K, Ishihara Y, Todaka T. A proposal for rotating machineries analysis by considering the unknown equal condition on fem. IEEE Trans Magn 1995;31(3):1722–4.
[29] McCalla WJ. Fundamentals of computer-aided circuit simulation. Norwell: Kluwer Academic Publishers; 1988.
[30] Wang JS, Ostergaard DF. A finite element-electric circuit simulation method for piezoelectric transducer. IEEE Ultrason Symp 1999;2:1105–8.
[31] Yoon GH. Topology optimization for stationary fluid–structure interaction problems using a new monolithic formulation. Int J Numer Methods Eng 2010;82:591–616.
[32] Chang SH, Rogacheva NN, Chou CC. Analysis of methods for determining electromechanical coupling coefficient of piezoelectric elements. IEEE Trans Ultrason Ferroelect Freq Control 1995;42(4):630–40.
[33] Trindade MA, Benjeddou A. Effective electromechanical coupling coefficients of piezoelectric adaptive structures: critical evaluation and optimization. Mech Adv Mater Struct 2009;16(3):210–23.
[34] Svanberg K. The method of moving asymptotes – a new method for structural optimization. Int J Numer Methods Eng 1987;24(2):359–73.